The Influence of Cr on Microstructural Evolution of Alumina

Yathreb Shalabi

The Influence of Cr on Microstructural Evolution of Alumina

Research Thesis

In Partial Fulfillment of the

Requirements for the Degree of

Master of Science in Materials Engineering

Yathreb Shalabi

Submitted to the Senate of

the Technion-Israel Institute of Technology

Nissan 5783 Haifa March 2023

The research thesis was done in the department of Materials Science and Engineering under the supervision of **Prof. Wayne D. Kaplan.**

The author of this thesis states that the research, including the collection, processing and presentation of data, addressing and comparing to previous research, etc., was done entirely in an honest way, as expected from scientific research that is conducted according to the ethical standards of the academic world. Also, reporting the research and its results in this thesis was done in an honest and complete manner, according to the same standards.

Acknowledgments

I would like to express my gratitude to my supervisor prof. Wayne D. Kaplan, who guided me throughout this work. The generous financial help of VATAT scholarship program for Arab society Master Research Track Students and the Technion is gratefully acknowledged.

Table of Contents

Abstract…….. 1

List of Symbols an Abbreviations 2

1. Literature Survey 4

1.1 Ceramic Processing 4

1.1.1 Solid State Sintering 4

1.1.2 Grain Growth/Coarsening 5

1.1.3 Grain Growth Mechanism 6

1.2 The Influence of Dopants on Grain Boundary Mobility 7

1.2.1 Solute-Drag 7

1.2.2 Zener Drag 9

1.3 Alumina 12

1.4 The Influence of Dopants on Alumina Grain Boundary Mobility 13

1.4.1 Mg Doped Alumina 13

1.4.2 Ca Doped Alumina 14

1.4.3 Si Doped Alumina 15

1.4.4 Co Doped Alumina 15

1.4.5 Cr Doped Alumina 16

2. Research Goals 17

3. Experimental Methods 18

3.1 Specimen Preparation 18

3.1.1 Undoped Alumina 18

3.1.2 Cr Doped Alumina 18

3.1.3 Mg Doped Alumina 18

3.1.4 Alumina Co-doped with Cr and Mg 19

3.2 Thermal Annealing 19

3.3 Characterization 19

3.3.1 Density 19

3.3.2 Wavelength Dispersive Spectroscopy (WDS) 19

3.3.3 Scanning/Transmission Electron Microscopy 21

3.3.4 Grain Size Grain boundary mobility Analysis 22

4. Results 24

4.1 The Actual Amount of Chromium 24

4.2 Microstructure 25

4.3 Grain Boundary Mobility 27

4.4 Occluded Pores 30

4.5 Grain Boundary Excess of Cr 31

5. Discussion 34

5.1 The Influence of Chromium on Densification of Alumina 34

5.2 The Influence of Chromium on The Grain Boundary Mobility of Alumina 35

5.3 The Influence of Chromium on Pore Mobility 36

6. Summary and Conclusions 39

7. Recommendations for Future Work 40

8. References 41

List of Figures

Figure 1: Fundamental microstructural changes which occur during sintering. 5

Figure 2: Schematic drawing of atoms migrating from one orientation to the other, resulting in the movement of the GB. 6

Figure 3: Schematic illustration showing the TLK model, terraces, ledges (steps), kinks, adatoms and vacancies. Reproduced from [6]..... 7

Figure 4: Schematic representation of the solute drag mechanism in crystalline ceramics. (a) is a symmetrical distribution of the dopant in the region of a stationary grain boundary, (b) is an asymmetric distribution produced by the moving boundary, and (c) is breakaway of the boundary from the dopant leaving a metastable solute cloud behind. Redrawn from [7]. 8

Figure 5: Driving force velocity behavior for (a) intrinsic migration, (b) solute drag only, and (c) total force velocity. Reproduced from [12]. 9

Figure 6: Interaction between a grain boundary and an immobile particle where in (a) the boundary approaches the particle, (b) there is interaction between the grain boundary and the particle leading to a retarding force on the boundary, and (c) describes the detailed geometry of the particle–grain boundary interaction. Reproduced from [7]. 10

Figure 7: Pore boundary interaction as a function of grain and pore size, assuming pores migrate by surface diffusion [13]. 11

Figure 8: The interface between the prismatic plane of sapphire which was diffusion bonded to MgO doped alumina. (a) Pore drag at the interface; and (b) pore separation and occlusion during growth of prismatic plane [14]. 12

Figure 9: Schematic drawing of the hexagonal (a) and rhombohedral (b) unit cells of α-alumina. The blue spheres represent aluminum cations, and the red spheres represent oxygen anions [17]..... 13

Figure 10: SE SEM micrographs (polished and cross-sectioned) of the microstructure of a) undoped alumina; b) Mg doped alumina; c) Co doped (Mg and Cr) alumina; d) 6171 ppm Cr doped alumina annealed for 0 h in air at 1600°C. 26

Figure 11: SE SEM micrographs (polished and cross-sectioned) of the microstructure of Cr-doped alumina after annealing for 2h in air at 1600°C which found to be saturated with Ca that caused a) elongated grains; and b) a secondary phase which is likely CA6. 27

Figure 12: SE SEM micrographs (polished and cross-sectioned) of the microstructure of Cr-doped alumina (6171 ppm) annealed for (a) 0 h and (b) 5 h at 1600°C in air. 27

Figure 13: Grain growth kinetics of undoped alumina and different Cr doped alumina samples annealed at 1600℃ in air. The slopes represent the values of the effective mobility of the different samples. 28

Figure 14: Grain growth kinetics of Mg-alumina, 91 ppm Cr-doped alumina, and co-doped alumina (132 ppm Mg and 126 ppm Cr). The slopes represent the values of the effective mobility of the different samples. 29

Figure 15: (a) SE SEM micrograph of Cr-doped alumina (8328 ppm Cr) demonstrating pores which detached from moving grain boundaries and became occluded within alumina grains. (b) Bright field TEM micrograph of Cr-doped alumina (8328 ppm Cr) showing an occluded and faceted pore. 30

Figure 16: STEM micrographs of (a) a pore at a grain boundary, (b) occluded pores and (c) a pore at a triple junction. 32

Figure 17: STEM micrograph of the grain boundary, showing regions for STEM-EDS analysis for the spatial difference method. 33

Figure 18: EDS line-scan across the pore surface indicated by the arrow in Figure 16(c). 33

Figure 19: Microstructure development map for alumina illustrating the effect of raising the surface diffusivity and reducing the grain-boundary mobility. Redrawn based on [62] and the behavior of Cr doped alumina was added to this figure in red. 38

List of Tables

Table 1: Summary of the dopant/impurity concentration in the samples including their measured detection limits. 24

Table 2: The alumina samples characterized in this study. 25

Table 3: Summary of the effective mobility measured for the samples in this study. 29

Table 4: The number density of occluded pores as a function of annealing time. 31

Table 5: The excess of Cr at grain boundary/ surface of the pore with the calculated detection limit of Cr. 31

Abstract

An important microstructural feature of polycrystalline materials is grain size, since grain size and the respective area of grain boundaries affect mechanical and functional properties. As such, grain growth plays a significant role in microstructural evolution during sintering of polycrystalline materials.

One of the most studied ceramic materials is α-alumina (α-Al_2O_3), which has served as a paradigm for the study of grain growth and is important for technological applications. Many studies showed that dopants and/or impurities can cause significant changes to the grain boundary mobility of materials. This can occur by equilibrium (Gibbsian) segregation of solutes to grain boundaries, which is driven by a reduction in grain boundary energy. The segregated solutes may then induce solute-drag or solute-acceleration, changing the grain boundary mobility and how the microstructure evolves. Alternatively, above the solubility limit, dopants and/or impurities can result in precipitation of secondary phases, which either reduce grain boundary mobility by Zener drag, or accelerate mobility by the formation of liquid phases.

This study investigates how Cr affects the effective mobility of grain boundaries in alumina. Considering that Cr_2O_3 is completely soluble in alumina, we are able to study the solute-drag (or solute-acceleration) phenomenon over a wide range of concentrations. As compared with undoped alumina, Cr-doped alumina has a reduced effective mobility. This includes co-doped samples (Mg/Cr), where Mg is known to reduce grain boundary mobility by solute drag. Furthermore, Cr-doped alumina was found to have significantly more occluded pores than Mg-doped or undoped alumina. As it will be discussed in this work, the mechanism by which chromium inhibits densification is by enhanced pore detachment, apparently due to a decrease in surface diffusivity.

List of Symbols an Abbreviations

I_{Bg}	Background intensity
C_{∞}	Bulk solute concentration
C_{std}	Concentration of element of interest in the standard
g_{ZAF}	Correction factor for atomic number, absorption, and fluorescence
ρ	Density
ψ	Dihedral angle
F_Z	Drag force of a single particle
β	Drift velocity
F_b	Driving force per unit area for boundary motion
D	Dry weight
γ_{GB}	Grain boundary energy
V_{GB}	Grain boundary velocity
G	Grain size
$C_{\mathrm{lim},0.95}$	Limit of detection (at a confidence larger than 95%)
τ	Measurement time
T_m	Melting temperature
M_{GB}	Mobility of a grain boundary
m	Number of measurements
ppm	parts per million
N_Z	Pore density at the grain boundary
V_P	Pore velocity
P	Pressure
k	Ratio of intensity of characteristic X-ray radiation measured from the sample to that measured from the standard
F_r	Retarding force
W	Saturated weight
SEM	Scanning electron microscopy
$STEM$	Scanning transmission electron microscopy
SE	Secondary electrons

F_s	Solute drag
a_S	Solute drag force per unit velocity per unit solute concentration
σ_{Bg}	standard deviation of the background intensity
I_{std}	standard intensity
$t(P,f)$	student coefficient for the confident probability
γ	Surface/interface energy
S	Suspended weight
A	Total interface area
TEM	Transmission electron microscopy
WDS	Wavelength dispersive X-ray spectroscopy
I	X-rays intensity

1. Literature Survey

1.1 Ceramic Processing

1.1.1 Solid State Sintering

Ceramics are typically manufactured through a sintering process which involves heating the material to a temperature below its melting point. This is because it is often challenging to achieve temperatures that are high enough to melt most ceramic materials. During sintering, the temperature is typically maintained within a range of 0.5Tm to 0.8Tm, where Tm represents the melting temperature of the material. This temperature range enables sufficient atomic mobility to occur, allowing the particles to bond together. The driving force behind the sintering process is the reduction of the total surface or interfacial energy of the system equation (1).

$$\Delta(\gamma A) = \Delta\gamma A + \gamma\Delta A \qquad (1)$$

where, γ is the excess surface/interface energy of a particle, A is the total interface area, γA is the total interfacial energy of the compact powder. Therefore, the interfacial energy of a compacted powder $\Delta(\gamma$A) can be lowered in two ways (see Figure 1):

1. Densification; which leads to the reduction of pore size and an increase in density. This is achieved by the elimination of solid-vapor interfaces and the creation of new, lower energy solid-solid interfaces (i.e. grain boundaries). As a result, there is a reduction in the particle interfacial energy, $\Delta\gamma$.
2. Grain growth or coarsening; which can occur through a process known as Ostwald ripening [1], a phenomenon when large particles grow at the expense of smaller ones. During grain growth (coarsening), the total grain boundary area A is reduced, resulting in a lower total energy in the system, γA.

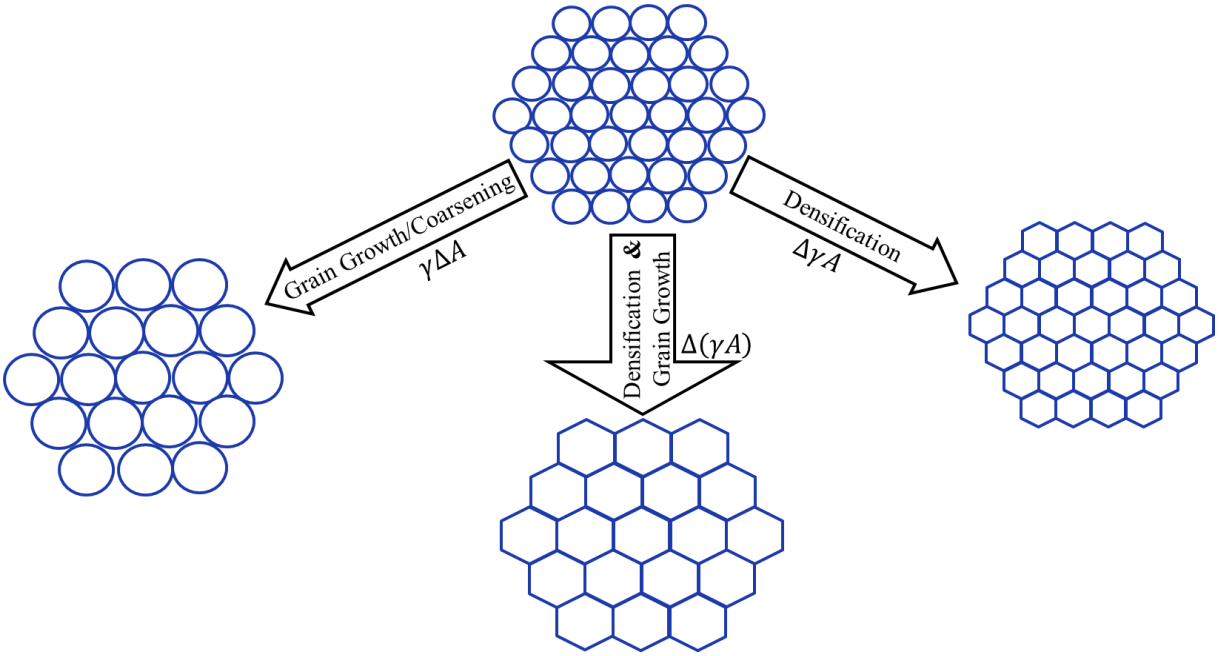

Figure 1: Fundamental microstructural changes which occur during sintering.

Densification and coarsening are two competitive processes that can occur simultaneously during sintering. When densification is the dominant process, the density of the compact powder increases due to pore shrinkage and eventual pore annihilation. However, when coarsening is dominant, both particles and pores grow over time. The balance between these two processes is critical to achieving the desired material properties and is an important area of study in the field of ceramics.

1.1.2 Grain Growth/Coarsening

During the various stages of densification, a significant amount of grain growth can occur. To reduce the overall grain boundary area and, consequently, decrease the excess energy of the system, grain boundaries migrate. This short-distance diffusionional process occurs as atoms move “across” the grain boundary when they change their orientation from that of the small crystal to that of the growing crystal. The movement of atoms results in a net flux in the opposite direction of grain boundary migration (Figure 2). During grain growth, the driving force for migration is typically described by the curvature of the grain boundary. This curvature results in a difference in chemical potential between the two grains, with convex grains having a higher chemical potential than concave grains equation (2).

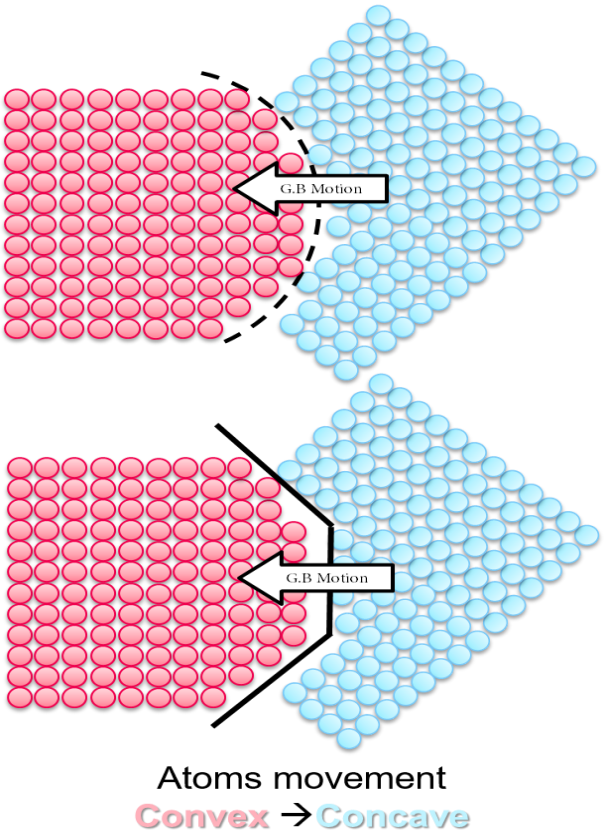

Figure 2: Schematic drawing of atoms migrating from one orientation to the other, resulting in the movement of the GB.

$$\Delta P = \gamma_{GB}\left(\frac{1}{r_1} + \frac{1}{r_2}\right) = \frac{n\gamma_{GB}}{\mathrm{G}} \qquad (2)$$

where ΔP the difference in pressure between adjacent grains, γ_{GB} is the grain boundary energy, n is a geometric factor and G is the grain size.

1.1.3 Grain Growth Mechanism

With the improvement of microscopy techniques, it was found that grain boundaries are faceted rather than curved. Gleiter suggested a migration mechanism based on the terrace-ledge-kink (TLK) model for surfaces (Figure 3), which involves the lateral motion of linear defects within the plane of the grain boundary [2]. These defects can have both step or/and grain boundary dislocation characteristics, and they are called disconnections [3]. During grain growth, atoms from the steps of the shrinking grain are adsorbed onto the steps of the growing grain. Although the TLK model was originally developed for crystal growth from the liquid or vapor phase, it has been applied to grain growth suggesting diffusion of atoms to the grain surface which later attach to step sites and finally diffuse at the step to a kink site.

Sternlicht et al. used transmission electron microscopy (TEM) to demonstrate that anisotropic disconnection motion is the mechanism of grain growth (in $SrTiO_3$ polycrystals) and recently Slorovitz extensively modeled the role of disconnections in grain growth [4,5].

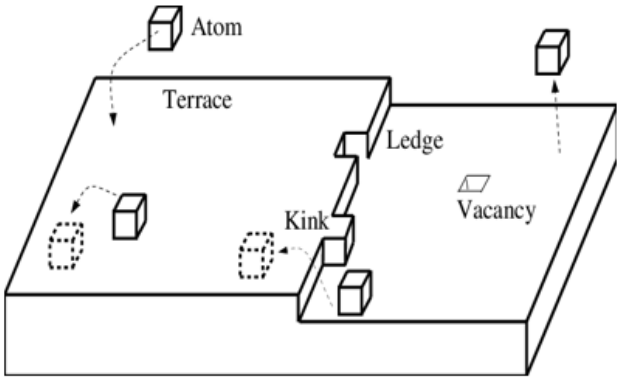

Figure 3: Schematic illustration showing the TLK model, terraces, ledges (steps), kinks, adatoms and vacancies. Reproduced from [6].

1.2 The Influence of Dopants on Grain Boundary Mobility

1.2.1 Solute-Drag

Below the solubility limit of a solute its atoms can adsorb (Gibbsian segregation) to grain boundaries and create a non-uniform chemical (and structural) distribution due to an interaction potential with the boundary. This segregation is driven by a reduction in the energy of the boundary. Figure 4(a) illustrates a symmetric distribution of solute ions at a grain boundary, where the charge is balanced by a space charge. When a grain boundary begins to move, the solute distribution that was initially symmetric becomes asymmetric due to differences in diffusivity between the solute ions and the host atoms. This asymmetric distribution creates an asymmetrical solute profile which has been proposed to result in a solute drag force (Fs) on the boundary. This drag force reduces the mobility of the boundary (see Figure 4 (b)). When the force driving the boundary migration is sufficiently strong, it has been proposed that the grain boundary velocity can become faster than that of the solute cloud, resulting in the boundary breaking away from the localized high concentration of solute as shown in Figure 4 (c).

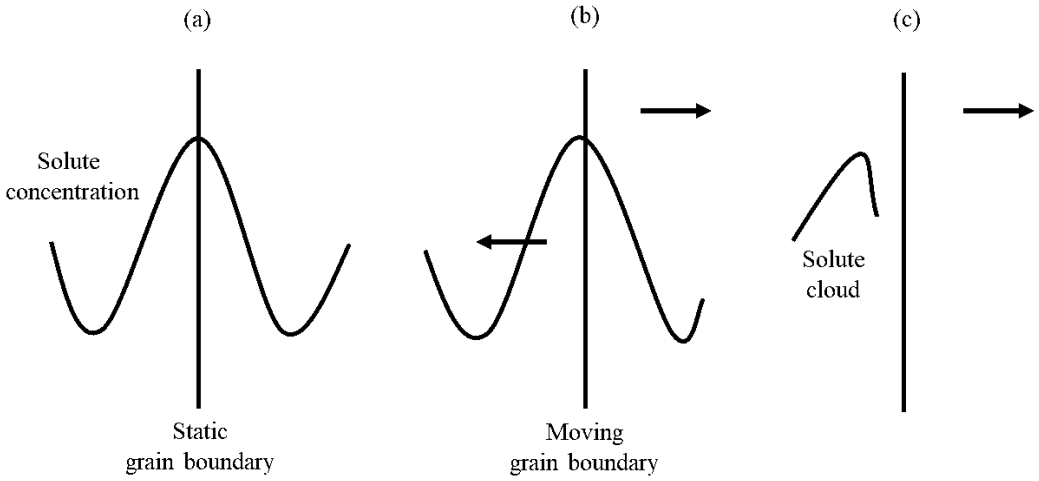

Figure 4: Schematic representation of the solute drag mechanism in crystalline ceramics. (a) is a symmetrical distribution of the dopant in the region of a stationary grain boundary, (b) is an asymmetric distribution produced by the moving boundary, and (c) is breakaway of the boundary from the dopant leaving a metastable solute cloud behind. Redrawn from [7].

Several models have been proposed to describe the solute drag force, as mentioned in references [8, 9, 10]. One of the models, proposed by Cahn, provides a calculation of the solute drag force (F_s) with respect to the distance from the grain boundary [11]:

$$F_s = \frac{\alpha_s C_\infty V_{GB}}{1 + (\beta V_{GB})^2} \qquad (3)$$

where α_s is the solute drag per unit velocity and per unit dopant concentration in the low boundary velocity limit, β is the drift velocity with which an impurity diffuses across the grain boundary, and C_∞ is the bulk solute concentration.

Regardless of whether the interaction between a solute and a grain boundary is attractive or repulsive, α_s will have a similar value if the interaction energy is the same. In steady state, the total drag force on the grain boundary is made up of two components: the intrinsic drag force (F_0) and the solute drag force (F_s) as described in Figure 5.

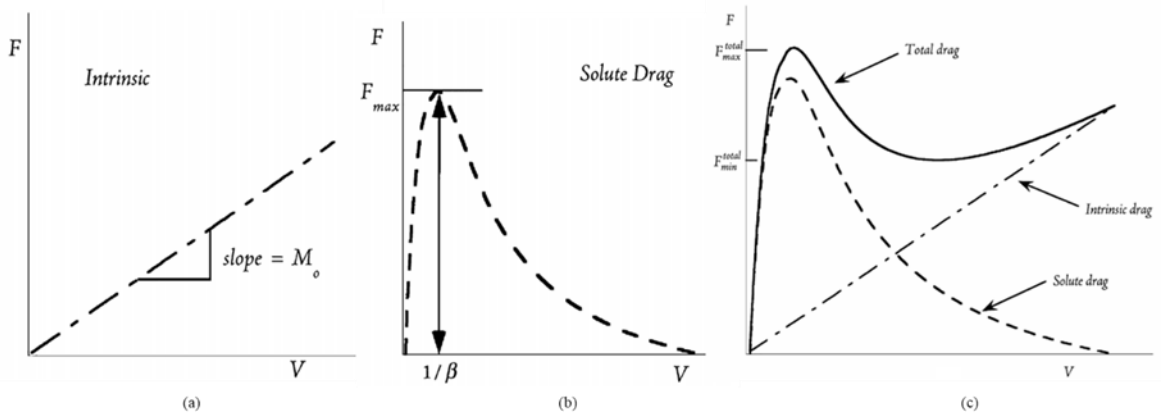

Figure 5: Driving force velocity behavior for (a) intrinsic migration, (b) solute drag only, and (c) total force velocity. Reproduced from [12].

Although this model explains how a decrease in mobility is expected when solute is introduced to the system, it is limited and does not presume to account for *solute acceleration*.

1.2.2 Zener Drag

When the dopant/impurity concentration is above the solubility limit, precipitation in the form of second phase particles will occur at equilibrium. The process may also be accompanied by enrichment which must be distinguished from equilibrium (Gibbsian) segregation. Enrichment is driven by expulsion of solute to the surface because of a total concentration which is above the equilibrium solubility limit, but kinetically limited precipitation may not yet occur.

Zener was the first to develop a quantitative model that explains particle-inhibited grain growth. In his model, he considered the particles to be randomly distributed in the polycrystalline solid, and assumed that they are spherical, insoluble, and immobile [7]. He then evaluated the driving force per unit area for boundary motion by taking a grain boundary with principal radii of curvature:

$$F_b = \gamma_{GB}\left(\frac{1}{a_1} + \frac{1}{a^2}\right) \qquad (4)$$

where F_b is the driving force, γ_{GB} is the grain boundary energy, a_1 and a_2 are the radii of curvature.

Assuming that a_1 and a_2 are proportional to the grain size G, then

$$F_b = \frac{\alpha\gamma_{GB}}{G} \qquad (5)$$

where α is a geometrical shape factor.

When the grain boundary intersects a particle, as presented in Figure 6, its movement is hindered and a retarding force acts on the boundary:

$$F_r = (\gamma_{GB} cos\psi)(2\pi r sin\psi) \quad (6)$$

where F_r is the retarding force, r is the radius of the inclusion and ψ is the dihedral angle.

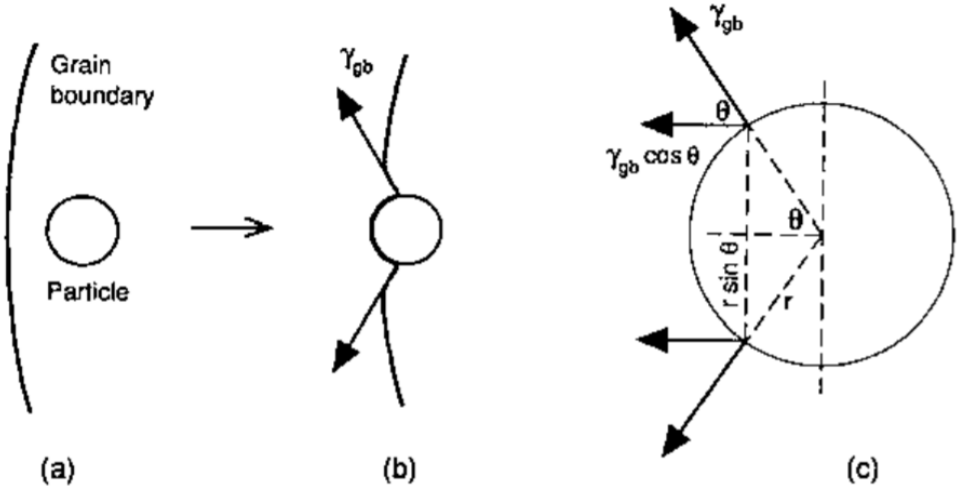

Figure 6: Interaction between a grain boundary and an immobile particle where in (a) the boundary approaches the particle, (b) there is interaction between the grain boundary and the particle leading to a retarding force on the boundary, and (c) describes the detailed geometry of the particle–grain boundary interaction. Reproduced from [7].

The presence of a particle at a boundary can result in a pinning force that exerts a drag on the boundary. The influence of a pore on grain boundary mobility can be treated in an identical manner as the influence of second phase [13]. This is why it is critical to work with dense materials when measuring grain boundary mobility (>95% density), where the amount of pores is insignificant.

The interaction between a pore and grain boundary can be treated in the following ways:

1. Separation of a pore from a grain boundary occurs when the velocity of the grain boundary exceeds a critical value which is the pore velocity ($V_{GB} > V_P$). This condition can be expressed in terms of the driving force as follows:

$$F_{GB} > N_Z F_Z + \frac{F_Z M_P}{M_{GB}} \qquad (7)$$

where N_Z is the pore density at the grain boundary, F_Z the drag force of a single particle M_P is the mobility of a spherical pore, M_{GB} is the mobility of a grain boundary and V_P is the pore velocity. Separation depends on the pore density and their mobility, which is inversely proportional to the pore radius to the fourth power as shown in Figure 7 .

2. As long as the pores are attached to the grain boundary, they both migrate with the same velocity ($V_{GB} = V_P$). It can be expressed in terms of the grain boundary velocity as:

$$V_{GB} > F_{GB}\left(\frac{M_{GB} M_P}{N_Z M_{GB} + M_P}\right) \qquad (8)$$

Equation (8(8) can be divided into two conditions:

i. When $N_Z M_{GB} \ll M_P$which means the pore has no effect on the migration rate of the grain boundary, also called boundary control.

ii. When $N_Z M_{GB} \gg M_P$ which means migration of the grain boundary is limited by the mobility of the pore, also called pore control.

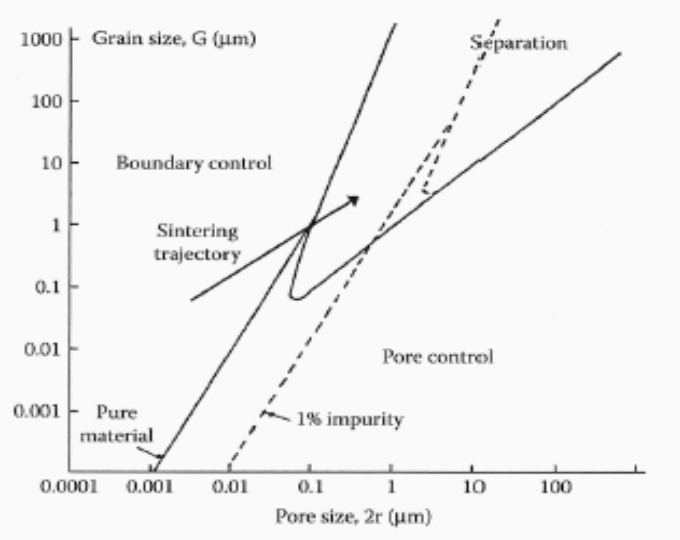

Figure 7: Pore boundary interaction as a function of grain and pore size, assuming pores migrate by surface diffusion [13].

For the case where separation of the pore from the grain boundary occurs, as shown for example in Figure 8, the pore will be trapped as an occluded pore inside the grain itself. This phenomenon of occluded pores is unwanted since the pores can only be removed by bulk diffusion.

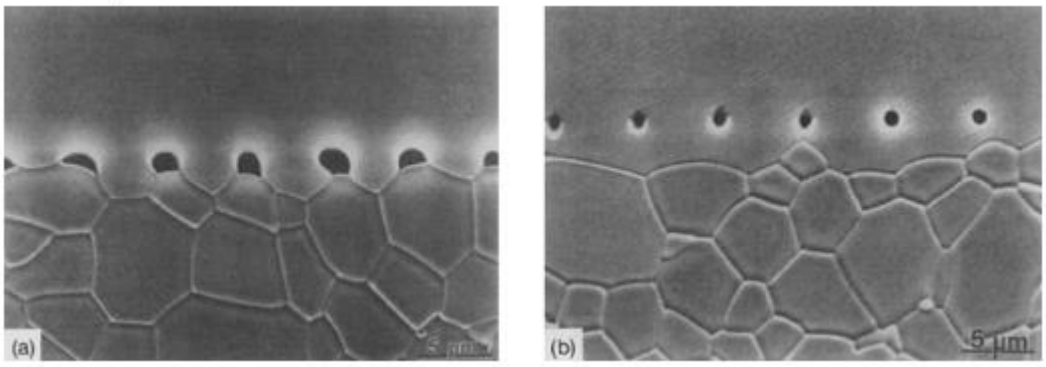

Figure 8: The interface between the prismatic plane of sapphire which was diffusion bonded to MgO doped alumina. (a) Pore drag at the interface; and (b) pore separation and occlusion during growth of prismatic plane [14].

The presence of dopants and impurities can have a significant impact on the mobility of grain boundaries in materials, either through solute drag/acceleration or Zener drag. Adsorbed dopant atoms can cause solute drag/acceleration below the solubility limit, whereas second-phase particles precipitated above this limit can pin the grain boundaries through Zener drag. In order to better understand the contribution of each mechanism to grain boundary drag, it is preferable to conduct fundamental studies *below* the solubility limit since it is difficult to isolate the individual effects of adsorbed solutes and Zener drag.

1.3 Alumina

Alumina (Al_2O_3) has several metastable structures, where α-alumina (corundum) is assumed to be the thermodynamically stable structure [15]. α-alumina possesses a trigonal symmetry with rhombohedral Bravais centering (space group $R\,\bar{3}\,C$ (No. 167)) and has 10 atoms in the unit cell. However, it is common to represent α-alumina using a hexagonal unit cell, which following Kronberg contain 30 atoms; 12 aluminum atoms and 18 oxygen atoms [16].

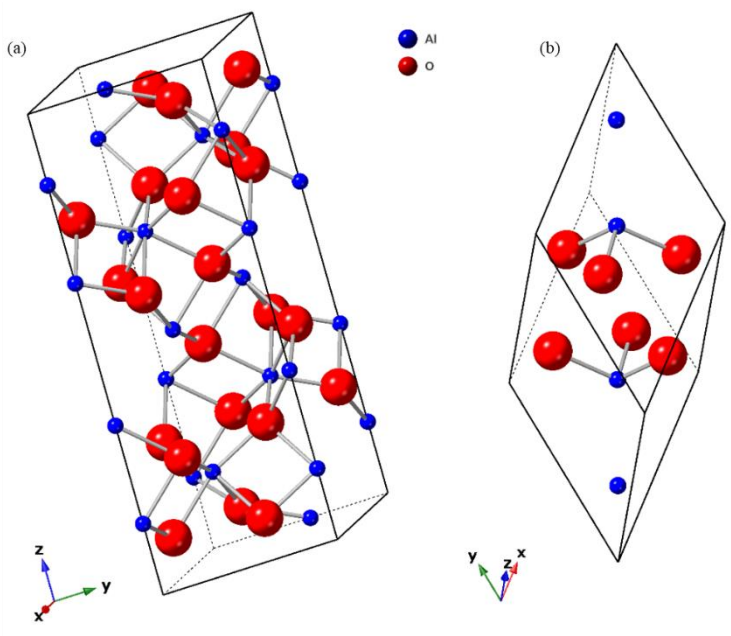

Figure 9: Schematic drawing of the hexagonal (a) and rhombohedral (b) unit cells of α-alumina. The blue spheres represent aluminum cations, and the red spheres represent oxygen anions [17].

α-alumina is a paradigm for oxide ceramics mostly due to its application in corrosive environments, resistance to abrasion, reasonable fracture strength, etc.

1.4 The Influence of Dopants on Alumina Grain Boundary Mobility

Measuring the grain boundary mobility of ceramics can be challenging because truly pure ceramics are difficult to produce. Even the powder used to sinter a ceramic material contains some level of impurities, which can affect the mobility of the grain boundaries. Despite this limitation, several studies have managed to measure the grain boundary mobility in undoped samples without directly addressing the influence of trace elements in the starting powder.

1.4.1 Mg Doped Alumina

The introduction of alumina in the ceramic industry initially resulted in poor densification after processing. However, Coble's work involving the addition of MgO as a dopant to alumina allowed for full densification to be achieved [18]. By sintering Mg-doped alumina under hydrogen, Coble successfully developed translucent polycrystalline alumina that could be used in high-pressure sodium lamps. Later it was found that Mg not only enabled full densification,

but also had the effect of minimizing abnormal grain growth, and reducing both grain boundary mobility and grain size [19,20,21].

The phase diagram of alumina and MgO does not show a solubility range for MgO in alumina [22]. Roy and Coble previously reported that the solubility limit of MgO in alumina was 300 ppm at a temperature of 1630°C, but they did not determine the actual Mg concentration after sintering in their work [20]. In a subsequent study, Miller et al. used quantitative wavelength dispersion spectroscopy (WDS) to investigate the solubility limit of MgO in alumina at 1600°C, and found it to be 132 ± 11 ppm [23].

Bennison and Harmer reported lower grain boundary mobilities in alumina resulting from the addition of Mg [24]. Specifically, they observed a decrease in mobility from$1.74x10^{-19}$ m^3/sec for undoped alumina to$3.9x10^{-20}$ m^3/sec for alumina doped with 200 ppm of Mg (concentration measured *before* sintering). Rödel and Glaeser similarly showed a decrease in the grain growth constant K from $28.5 \cdot 10^{-3}\text{sec}^{-1}$ for undoped alumina to $7.1 \cdot 10^{-3}\text{sec}^{-1}$ for alumina doped with 250 ppm of Mg (concentration measured *before* sintering) [21].

The solubility limit of MgO in alumina was used to investigate the influence of MgO on the grain boundary mobility of alumina. In particular, Akiva et al. examined the effects of Mg on the mobility of alumina at a concentration of Mg that was experimentally verified to be below the solubility limit. Their results demonstrated a decrease in grain boundary mobility due to the solute drag effect [25].

1.4.2 Ca Doped Alumina

Despite the solute drag effect Mg has, some experimental evidence suggests that impurities present in concentrations below their solubility limit can actually increase the grain boundary mobility. Doping alumina with CaO has been shown to increase grain growth and grain boundary mobility by accelerating the movement of grain boundaries [26]. However, it is difficult to determine whether the increased grain boundary mobility is due to equilibrium segregation or the precipitation of a second phase without knowledge of the solubility limit. The published phase diagram of alumina and CaO does not provide a solubility range for CaO in alumina [27], similar to the situation with MgO. To address this, Akiva et al. used the WDS technique developed by Miller et al. to measure the solubility limit of CaO in alumina at 1600°C. Their findings showed that the solubility limit of CaO in alumina is 51 ± 1 ppm. Afterwards it was experimentally demonstrated that doping alumina with CaO below the

solubility limit resulted in increased grain boundary mobility from $2.65 \cdot 10^{-15} \frac{m^2}{s}$ for undoped alumina to $3.48 \cdot 10^{-15} \frac{m^2}{s}$ for alumina doped with 13±1 ppm of Ca, contradicting the solute-drag effect which is expected when equilibrium segregation to grain boundaries occurs.

1.4.3 Si Doped Alumina

Bae and Baik conducted a study on Si-doped alumina and reported abnormal grain growth due to the formation of a liquid phase [28]. They found that doping alumina with Si above 300 ppm leads to abnormal growth. Lee and Kröger determined the solubility limit of Si in alumina at 1600°C by electrical conductivity measurements and found it to be 300 ppm [29]. Dillon and Harmer also reported an adsorption transition and a change in grain growth kinetics as a function of Si concentration [30]. In both studies, the actual Si concentration after sintering was not measured and without knowledge of the solubility limit, the mechanism by which Si affects the microstructure remains unknown.

Similar to MgO and CaO, the published phase diagram of alumina and SiO_2 does not provide information on the solubility range of SiO_2 in alumina. To address this, Moshe et al. used a fully standardized WDS technique to determine the solubility limit of SiO_2 in alumina at 1600°C. Their findings showed that the solubility limit of SiO_2 in alumina is 188 ± 7 ppm [31]. This information is crucial for understanding the mechanism behind the effect of Si on grain growth in alumina.

1.4.4 Co Doped Alumina

Co-doped alumina systems have also been a subject of many studies. Handwerker et al. investigated the influence of Mg on the grain growth of alumina in the presence of Ca and Si [32]. Their hypothesis was that Mg could increase the solubility limit of impurities such as Ca and Si, thereby preventing the formation of secondary liquid phases that may increase the rate of grain growth.

Furthermore, the influence of Mg on the solubility limits of Ca and vacancies in alumina was studied considering a system that contains them both [33]. It was found that the presence of Mg resulted in a decrease in the Ca solubility limit and an increase in the solubility limit of Mg in alumina due to the presence of Ca. These findings suggest that co-doping alumina with Mg and

Ca leads to a higher Mg concentration in the grains compared to Mg-doped alumina. Additionally, the increased amount of Mg excess exerting a solute-drag force on alumina grain boundaries leads to a decrease in grain boundary mobility.

1.4.5 Cr Doped Alumina

The pseudo-binary phase diagram of Al_2O_3- Cr_2O_3 shows that alumina forms a complete solid solution with Cr_2O_3 without any eutectic at 1600°C [34]. Moreover, when Cr^{3+} is incorporated into alumina, the difference in ionic radii between Al^{3+} (54 pm) and Cr^{3+} (62 pm) [35] causes compression of the 3d orbitals of chromium and leads to changes in electronic properties [36]. This manifests in a shift of the optical absorption maximum for Cr^{3+} from red to green, resulting in a color change from green in pure chromia to red in $(AlCr)_2O_3$ solid solutions with a few percent Cr^{3+} (ruby). The presence of Cr^{3+} in the solid solution can also cause residual stresses in the crystal lattice if only part of the Al^{3+} is replaced by Cr^{3+}.

Previous studies have examined the densification behavior of bulk Al_2O_3-Cr_2O_3 solid solutions and found that an increase in Cr^{3+} content leads to reduced densification, shrinkage, and the formation of residual porosity [37,38,39,40]. This is due to the vaporization/condensation of Cr_2O_3, and the extra thermal energy required for the creation of $(AlCr)_2O_3$ solid solutions [41].

Harabi and Davies reported that the density attainable for Cr doped alumina was limited by a residual porosity, which consisted entirely of closed pores in almost all compositions of Cr they studied [42]. A sintering study which was conducted on various Cr contents in alumina showed that densification increases with an increase in sintering time and temperature. However, densification tends to decrease with an increase in Cr content, showing a maximum density of 3.452 gr/cm^3 at 2.0 wt. % Cr at 1700 °C. The porosity of the compacts, rate constant and activation energy were reported to increase with an increase in Cr content [34]. Manor investigated the grain growth inhibition in nanocrystalline Al_2O_3 doped with Cr, which revealed distinct inhibition of grain growth in the presence of Cr [43].

Considering all the aspects cited above, including the fact that most of the studies mentioned did not experimentally determine the concentration of dopants used, the current research aims to examine how minor additions of Cr affect the microstructure evolution of 99.99% α-Al_2O_3.

2. Research Goals

The primary aim of this research is to provide answers for the following main questions:

- How does Cr affect the mobility of grain boundaries in alumina?
- Does Cr^{3+} segregate to the grain boundaries in alumina?
- How does co-doping (Mg/Cr) influence the grain boundary mobility?

To answer these questions, grain growth analysis was conducted on fully dense samples of undoped alumina and Cr/Mg doped alumina so as to neglect the pore drag effect.

3. Experimental Methods

3.1 Specimen Preparation

3.1.1 Undoped Alumina

Polycrystalline alumina samples were prepared using 150 gr of high purity (99.99%) α-Al_2O_3 powder (Ceralox HPA 0.5, Tucson, AZ, the size of the initial alumina particles was add is 300nm) which was mixed with 65 gr of distilled water. The alumina suspensions were deflocculated by reducing the pH of the slurry to a pH of ~4 by adding a small amount analytically pure HCl (well below the isoelectric point of alumina which is between pH of 8-9 [44]). The alumina suspension was mixed for 24 h using a ball-milling system but without milling balls to reduce contamination and this was done following the conclusions reached by Miller et al. regarding the use of ZrO_2 milling balls which introduced ~50 ppm of Zr into alumina grains [23]. Green bodies were formed by vacuum filtration, followed by drying in air for 24 h at room temperature, and then followed by drying at 80°C for 5 h and 110°C for 2 h. The green bodies were bisque-fired at 1000°C for 2 h in air (heating rate 15°C/min) so as to form necks at alumina contact points without changing the density. Sintering was conducted in air at 1600°C for 2 h resulting in dense samples (>95% relative density).

3.1.2 Cr Doped Alumina

Cr-doped alumina samples were prepared as mentioned above, with an additional infiltration process before the sintering stage. During the infiltration process the fired green bodies were placed in a beaker with a water-based Cr nitrate solution ($Cr(NO_3)_3)\cdot 6H_2O$, which was prepared by dissolving 130 gr Cr nitrate in 300 ml distilled water and placed in a vacuum desiccator for ~24 h. The beaker was then removed from the vacuum desiccator and heated to 60°C for 4 h in order to reduce the contact angle of the Cr nitrate with alumina and promoting infiltration [45]. The samples were then removed from the Cr nitrate solution, dried for 10 h at 35°C in air, and then dried for 5 h at 110°C in air, before sintering for 2 h at 1600°C (>95% relative density).

3.1.3 Mg Doped Alumina

Ready to press (RTP) polycrystalline alumina samples which contained Mg were prepared using alumina powder from Ceralox (AHPA-0.5, Sasol North America, AZ) with a purity of 99.995%. The powder was in the spray-dried, RTP form. The RTP alumina was doped with MgO (300 ppm) by the supplier. The powder was used in its as-received form. Alumina green bodies were prepared by uniaxial pressing at ~40 MPa, followed by CIP at 207 MPa. The green

bodies were bisque-fired at 1000°C for 2 h in air. The samples then were sintered at 1600°C for 2 h in air (>95% relative density).

3.1.4 Alumina Co-doped with Cr and Mg

RTP samples were prepared as mentioned above, with an additional infiltration process before the sintering stage as it described in section 3.1.2.

3.2 Thermal Annealing

Each fully dense "mother sample" which was prepared as described in section 3.1 was cut into pieces, where each piece underwent annealing in air at different times (0 h -5 h) at 1600°C to promote grain growth.

3.3 Characterization

3.3.1 Density

The density of each mother sample was measured using the Archimedes method following ASTM standard c 20-92.

$$\rho = \left(\frac{D}{W-S}\right) \cdot \frac{1}{\rho_{Al_2O_3}} \qquad (9)$$

where D is the dry weight, W is the saturated weight, S is the suspended weight and $\rho_{Al_2O_3}$ is the theoretical density of alumina which is 3.97 gr/cm^3.

3.3.2 Wavelength Dispersive Spectroscopy (WDS)

The solute concentrations were measured using WDS (Oxford Instruments, High Wycombe, U.K.) mounted on a scanning electron microscope (FEI E-SEM Quanta 200, Eindhoven, Holland). WDS measurements were acquired at a working distance of 11 mm, a magnification of x10,000, a spot size resulting in a probe current of at least ~70 nA, and a measurement time of 20 sec. An accelerating voltage of 20 kV was used to optimize between high signal intensity and low background intensity. A lithium fluoride (LiF) crystal was used as a monochromator

for the WDS measurements of Cr, and pure Cr was used as a standard. The elemental K_α peak was measured at a spectral position showing a maximum intensity. The background intensity was measured at two different spectral positions around the peak position. The background intensity in the peak position was calculated by linear interpolation. 30 measurements were taken from random locations across the cross each section for each element quantification.

For measuring the concentration of other dopants, a polyethylene terephthalate (PET) crystal was used as a monochromator for the measurements of Ca and Si, and a thallium acid phthalate (TAP) crystal for the measurements of Mg. Diopside $MgCaSi_2O_6$ was used as a standard for Mg, Ca and Si quantification.

The dopant's concentration was calculated according to:

$$C = k \cdot C_{std} \cdot g_{ZAF} \tag{10}$$

where C_{std} is the concentration of the standard (for a pure element C_{Std}=1), k is a constant describing the ratio between the measured intensities of the peak and it's background and g_{ZAF} correlates to the ZAF correction factor, where Z is the atomic number correction, A is the absorption correction, and F is the characteristic fluorescence correction. For the dopant content measurements, a ZAF correction factor was calculated using XPHI Software [46].

An element of interest is detected in a given specimen under the condition that the inequality $I > I_{Bg}$is fulfilled at a defined level of confidence probability (P):

$$I - I_{Bg} \geq t(P, f) \cdot \sqrt{2} \cdot \sigma_{Bg} \tag{11}$$

where $t(P, f)$ is a student coefficient for the confident probability P and a number of degrees of freedom f ($f = m - 1$). σ_{Bg} is the standard deviation of the background intensity and m is the number of measurements of the background intensity.

Taking a Poisson distribution for the background intensity, one can obtain a limit of detection for the element in question as [45,47]:

$$C_{\mathrm{lim},0.975} = C_{std} \cdot g_{ZAF} \cdot \frac{2\sqrt{2\mathrm{I}_{\mathrm{bg}}}}{\sqrt{m\tau} \cdot I_{std}} \quad (12)$$

where $C_{lim,0.975}$ is the limit of detection with a confidence probability of 97.5%. I_{bg} is the background intensity, C_{std} and I_{std} are the concentration and intensity from a standard with a known concentration, respectively, m is the number of measurements, and τ is the measurement time.

3.3.3 Scanning/Transmission Electron Microscopy

Scanning electron microscopy (SEM) and scanning/transmission electron microscopy (S/TEM) were used for microstructure characterization on polished cross-sectioned (conventional) samples.

SEM was conducted using an FEI Quanta 200 E-SEM (Eindhoven, Holland) and a Zeiss Ultra-Plus field emission gun SEM (Oberkochen, Germany). Specimens for SEM and WDS measurements were prepared by slicing and then mechanical polishing of the interior sections of each sample using a diamond suspension on polishing cloths, starting from a diamond size of 30 μm and concluding with a diamond size of 1 μm. After polishing, the samples were ultrasonically cleaned in acetone, ethanol and then rinsed in isopropanol. For the analysis of the grains' microstructure thermal annealing for grain boundary grooving was conducted in an air furnace at 1250°C for 2 h. For WDS measurements no chemical or thermal etching was performed on the samples used to prevent possible changes in concentration.

Further investigation of the microstructure and analysis of occluded pores was conducted by transmission electron microscopy (TEM, Tecnai T-20 G2 200kV, FEI, Eindhoven, Holland) and elemental analysis was done by scanning transmission electron microscopy (STEM) and energy dispersive spectroscopy (EDS, EDAX, Tilburg, Holland) using a monochromated and double aberration-corrected S/TEM (FEI Themis-Z 80–300 keV S/TEM) operated at 300 kV. TEM samples were prepared by conventional mechanical thinning (final thickness of ~100μm), followed by dimpling to ~30μm, and ion-milling (Gatan PIPS, Pleasanton, CA) with Ar at 4-8 kV until perforation.

For quantitative analysis of the amount of Cr at the boundary, energy dispersive spectroscopy (EDS, EDAX, Tilburg, Holland) using a monochromated and double aberration-corrected

S/TEM (FEI Themis-Z 80–300 keV S/TEM) operated at 300 kV was acquired from a region rastered with the electron beam having dimensions of 85.65nm x 101.5nm. The amount of Cr excess was defined as [48]:

$$\Gamma_{Cr} = \frac{V}{S} \cdot \rho_{Al_2O_3} \cdot k_{(Cr,Al)} \cdot \frac{2 \cdot A_{Al}}{A_{Cr}} \cdot \frac{I_{Cr}}{I_{Al}} \qquad (13)$$

where V/S is the ratio of the interaction volume to the area of the grain boundary inside the interaction volume, $\rho_{Al_2O_3}$ is the matrix density in atom/nm^3, and A_{Al}, A_{Ca}, I_{Al}, and I_{Ca} are the atomic masses and measured intensities for the Al and Ca species, respectively.

The detection limit at the grain boundary was define [48]:

$$\Gamma_{min} = \frac{V}{S} \cdot \rho_{Al_2O_3} \cdot k_{(Cr,Al)} \cdot \frac{2 \cdot A_{Al}}{A_{Cr}} \cdot \frac{3 \cdot \sqrt{2 \cdot I_{Cr}^{bg}}}{I_{Al}} \qquad (14)$$

where I_{Cr}^{bg} is the background intensity under the peak of interest. The $k_{(Cr,Al)}$ were determined experimentally from the bulk of Cr- doped alumina following the Cliff & Lorimer technique [49].

$$\frac{C_{Cr}}{C_{Al_2O_3}} = k_{Cr-Al} \cdot \frac{I_{Cr}}{I_{Al_2O_3}} \qquad (15)$$

where C_{Cr} and $C_{Al_2O_3}$ are the weight percent of each element when $C_{Cr} + C_{Al_2O_3} = 1$.

3.3.4 Grain Size Grain boundary mobility Analysis

Grain sizes were measured using a MatLab program following the linear intercept method [50], from > 600 grains in each sample. A correction factor of 1.57 was used to correlate between the average grain size $\bar{G}$ and the average intercept length $\bar{L}$, so $\bar{G} = 1.57 \cdot \bar{L}$.

Grain boundary mobility can be determined from the measured grain size as a function of annealing time, assuming equiaxed grains and $n = 2$ [12]:

$$\bar{G}_t^2 - \overline{G_{t=0}}^2 = 4M_{GB}\gamma_{GB}t = kt \quad (16)$$

where $\bar{G}_t^2$ is the average squared grain size at time t, $\overline{G_{t=0}}^2$ is the average squared grain size at t=0 and k is the rate constant.

Thus, the term effective mobility can be derived from equation (16) as:

$$M_{GB}\gamma_{GB} = \frac{k}{4} \quad (17)$$

Plotting a graph of the average grain size as a function of annealing time at a defined temperature, using equation(16), the rate constant K (the slope) can be converted to the effective grain boundary mobility using equation(17).

4. Results

4.1 The Actual Amount of Chromium

Determining the actual amount of impurities and dopants in the samples is crucial to understanding their influence on grain growth. During processing impurities can be introduced even at trace levels from the starting powder, molds, furnaces, and other lab equipment. In addition, dopants mixed into the powder or added in solution might evaporate during sintering, altering the intended dopant concentration.

To determine the actual concentration of an element, we have to determine the minimal concentration of that element that we can detect, this means determining the detection limit of the dopant. This was done considering each specific specimen, WDS/SEM operating conditions and the number of measurements conducted for each sample, using equation (12). The limits of detection for Mg, Ca and Cr in the different samples are presented in Table 1.

Table 1: Summary of the dopant/impurity concentration in the samples including their measured detection limits.

Sample	Dopant	Concentration [ppm]				Detection limit [ppm]
Undoped	Cr	1 ± 3				8
	Ca	1 ± 1				7
	Mg	4 ± 3				10
Cr-doped alumina	Cr	8328± 105	6171± 61	2343± 17	91± 9	7
	Ca	-	10 ± 6	2± 2	8 ± 2	11
	Mg	-	3 ± 1	2 ± 1	2 ± 1	9
RTP	Cr	5 ± 2				7
	Ca	-				-
	Mg	> 132				-
RTP+Cr	Cr	126 ± 6				7
	Ca	9 ± 4				16
	Mg	> 132				-

Then an effort to measure the actual concentration of key dopants (Ca, Mg, Cr) in the “mother” samples was conducted by WDS after sintering. The solubility limit of Ca, Mg and Cr in alumina at 1600°C is 51 ppm, 132 ppm and no limit, respectively [25, 23, 34]. The actual

concentration of each dopant/impurity and the measured relative density of the mother sample is presented in Table 2.

Mg was added to the powder by the supplier by the addition of high purity magnesium aluminate spinel. Even though the supplier reported a presence of 300ppm Mg in the RTP powder, after the thermal treatments that the samples underwent, we ended with a final concentration of Mg of ≥132 ppm (saturated plus isolated spinel precipitates). The microstructure of the Mg doped sample, which is presented in Figure 10 (b), showed a negligible amount of Mg spinel particles.

Table 2: The alumina samples characterized in this study.

Sample Label	Cr Concentration [ppm]	Mg Concentration [ppm]	Relative Density	Bright field optical micrograph
Undoped alumina	Below detection limit	Below detection limit	98.2 %	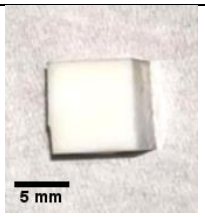
Cr-doped alumina	6171± 61	Below detection limit	96.1 %	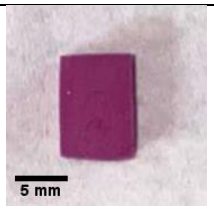
	2343± 17		97.3 %	
	91± 9		98.4 %	
Mg-doped alumina	Below detection limit	> 132	99 %	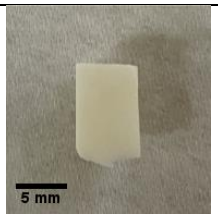
Co-doped alumina (Mg/Cr)	126 ± 6	> 132	97.4 %	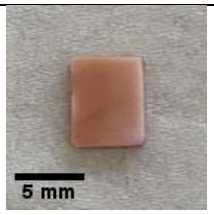

4.2 Microstructure

The microstructure of the undoped and doped polycrystalline alumina samples that were annealed for 0 hours (as sintered) in air at 1600°C are presented in Figure 10. It can be seen that all the samples are dense (>95% relative density).

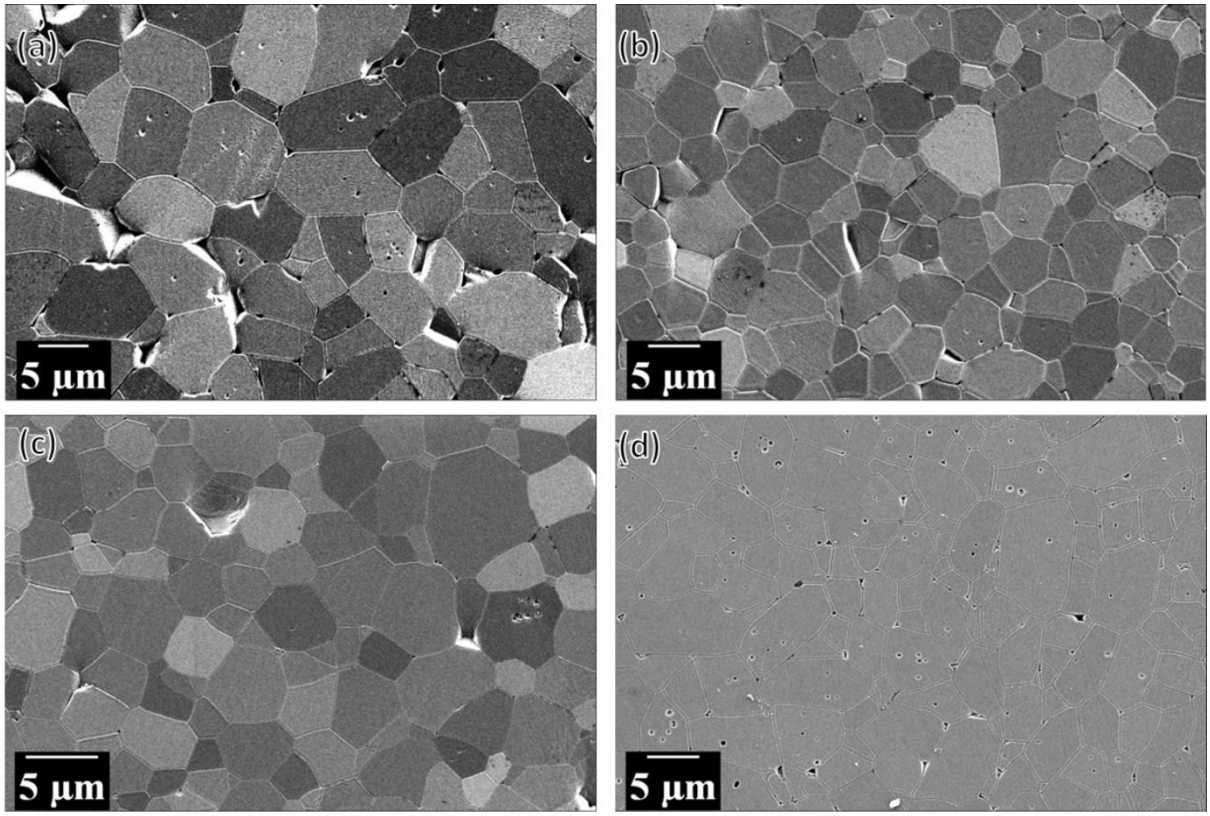

Figure 10: SE SEM micrographs (polished and cross-sectioned) of the microstructure of a) undoped alumina; b) Mg doped alumina; c) Co doped (Mg and Cr) alumina; d) 6171 ppm Cr doped alumina annealed for 0 h in air at 1600°C.

Figure 11 presents the microstructure of 2757 ppm Cr- doped alumina before and after annealing. First, the grains exhibit an elongated (plate-like) morphology. Second, the sample has two phases (after annealing). WDS measurements of Ca showed 60 ± 4ppm of Ca with a detection limit of 7 ppm and it is known that the solubility limit of Ca in alumina at 1600°C is 51 ppm. EDS measurements on the area indicated with a red arrow in Figure 11 indicate a significant peak of Ca. EDS in SEM does not have the sensitivity to detect Ca in alumina at the level of 60 ppm, thus the microstructure indicated in Figure 11 must be a secondary phase. Thus, the two phases are α-Al_2O_3 and apparently CA6 (calcia hexaaluminate; $CaO{\cdot}6Al_2O_3$) [25].

Since this sample was contaminated with Ca, it was not included in the analysis of grain boundary mobility. This case exemplifies the importance of determining the actual chemical content of the samples.

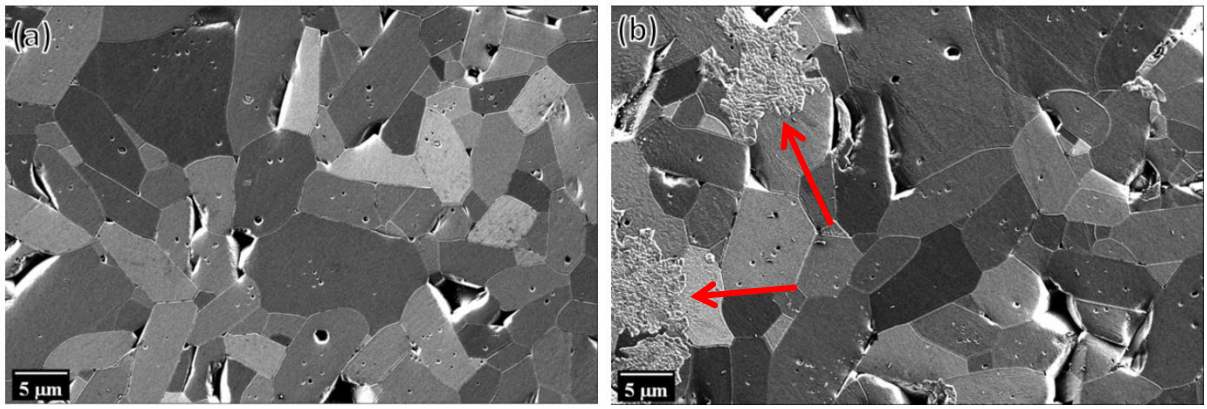

Figure 11: SE SEM micrographs (polished and cross-sectioned) of the microstructure of Cr-doped alumina after annealing for 2h in air at 1600°C which found to be saturated with Ca that caused a) elongated grains; and b) a secondary phase which is likely CA6.

4.3 Grain Boundary Mobility

The effective grain boundary mobility was determined by measuring the change in average grain size as a function of annealing time at 1600°C in air. Figure 12 shows an example of the change in the grain size after annealing a dense sample for a longer time. Grain growth kinetics of undoped and doped polycrystalline alumina samples annealed at 1600℃ in air are described in Figure 13Figure 14 . The small slope indicates a reduced effective mobility.

Considering parabolic grain growth kinetics (equation(16)) the results can be summarized in Table 3. The results show a trend where an increasing chromium content reduces the effective mobility. Moreover, the Mg doped sample was found to have a lower value of effective mobility compared with undoped alumina and 91 ppm Cr-doped alumina (the closest concentration to 132 ppm Mg). The influence of the co-doping doesn't significantly differ from the influence of Mg by itself.

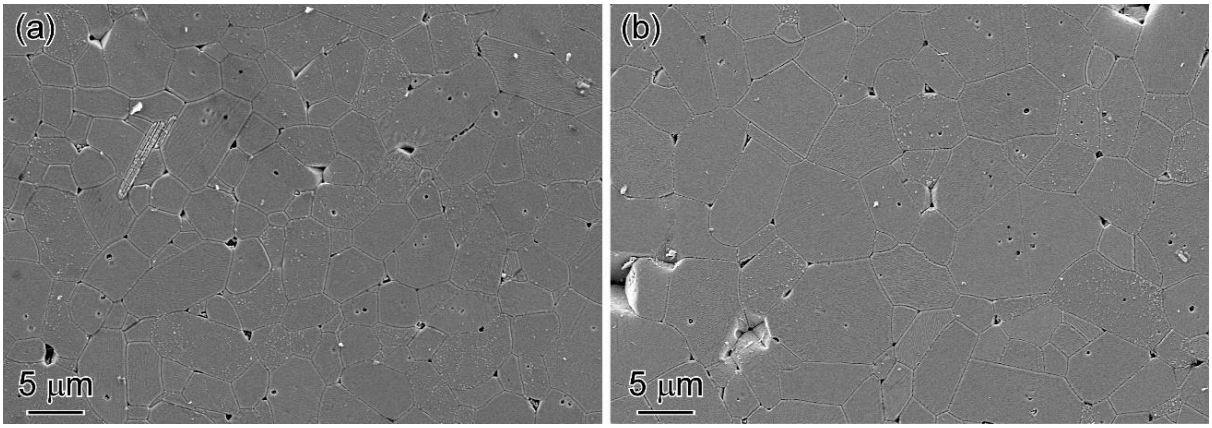

Figure 12: SE SEM micrographs (polished and cross-sectioned) of the microstructure of Cr-doped alumina (6171 ppm) annealed for (a) 0 h and (b) 5 h at 1600°C in air.

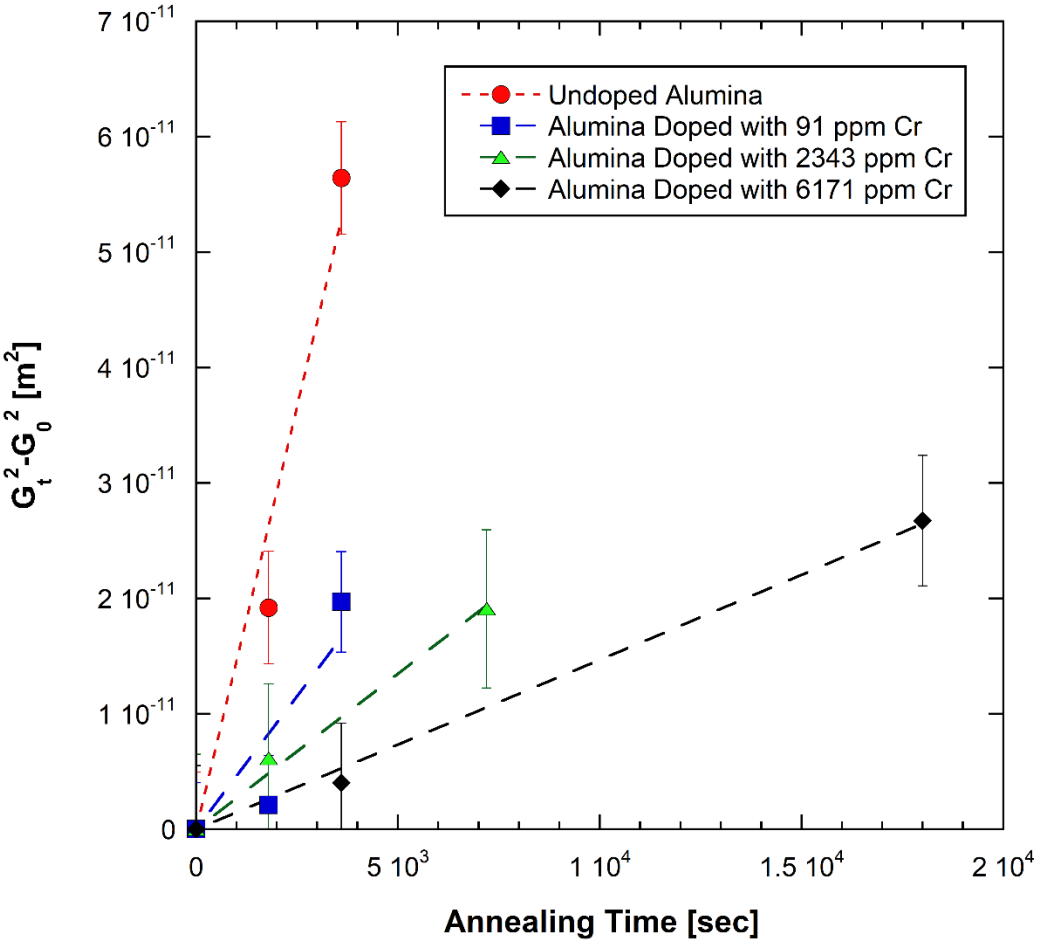

Figure 13: Grain growth kinetics of undoped alumina and different Cr doped alumina samples annealed at 1600℃ in air. The slopes represent the values of the effective mobility of the different samples.

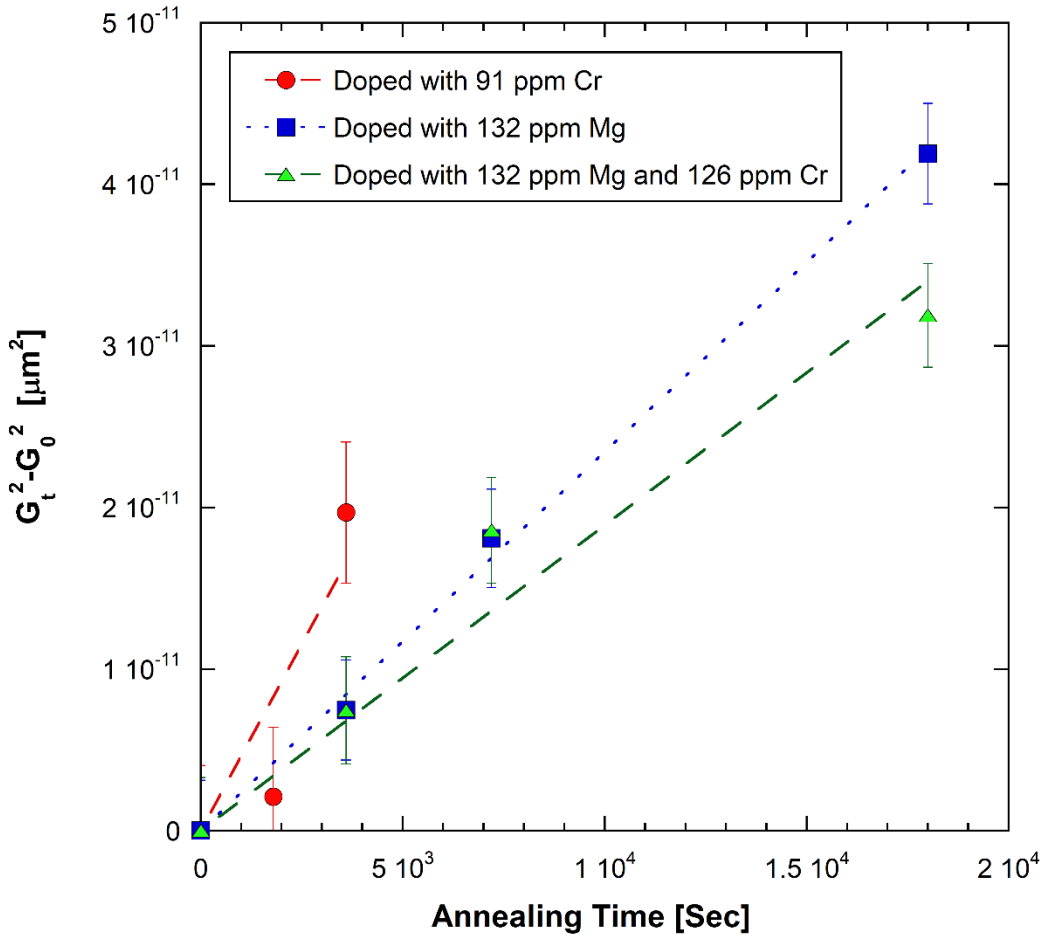

Figure 14: Grain growth kinetics of Mg-alumina, 91 ppm Cr-doped alumina, and co-doped alumina (132 ppm Mg and 126 ppm Cr). The slopes represent the values of the effective mobility of the different samples.

Table 3: Summary of the effective mobility measured for the samples in this study.

Sample	**Effective mobility [10^{-15} m^2/sec]**
Undoped alumina	3.67 ± 2.17
91 ppm Cr	1.15 ± 1.01
2343 ppm Cr	0.68 ± 0.54
6171 ppm Cr	0.37 ± 0.29
132 ppm Mg-doped alumina	0.58 ± 0.27
132 ppm Mg/126 ppm Cr (Co-doped alumina)	0.47 ± 0.23

The error values of the effective mobility were calculated considering the max value of the last point (with the error) of each sample, versus the lowest value.

4.4 Occluded Pores

During characterization of the microstructure of the samples using SEM and TEM, an interesting trend was found regarding the presence of occluded pores (indicated by arrows in Figure 15) in samples containing Cr. These samples have a higher occurrence of occluded pores compared to samples without Cr, (undoped alumina and Mg-doped alumina (RTP)).

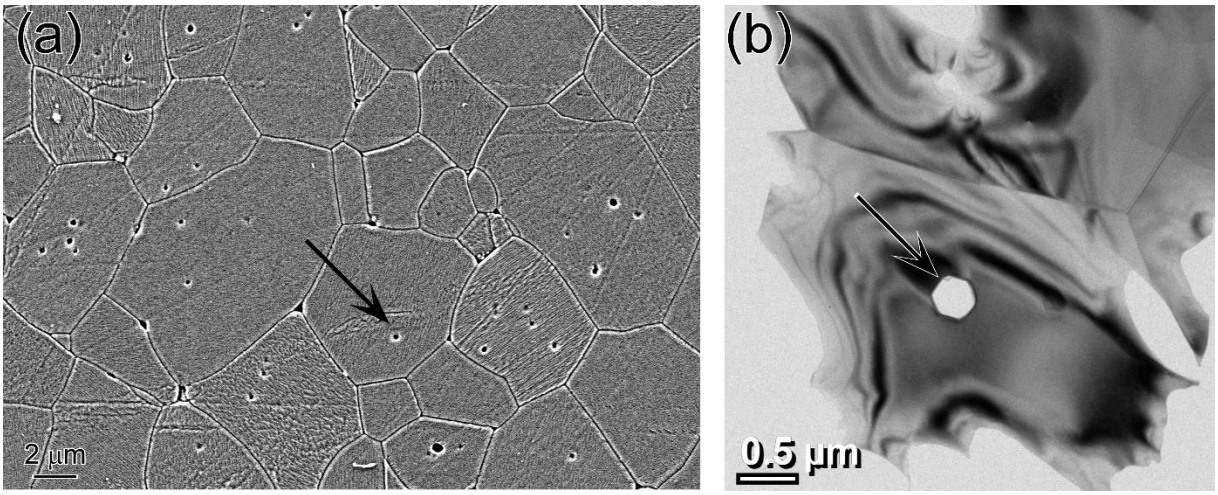

Figure 15: (a) SE SEM micrograph of Cr-doped alumina (8328 ppm Cr) demonstrating pores which detached from moving grain boundaries and became occluded within alumina grains. (b) Bright field TEM micrograph of Cr-doped alumina (8328 ppm Cr) showing an occluded and faceted pore.

To further investigate this observation, quantification of the number density of the occluded pores in more than 600 grains after extended annealing for Mg-doped alumina and Co doped alumina (Mg/Cr) was done. The number density of the occluded pores can be described as:

$$N_{density} = \frac{N_{occluded\ pores}}{N_{total\ pores}} \qquad (18)$$

where $N_{density}$ is the number density of the occluded pores, $N_{\text{occluded pore}}$ is the amount of occluded pores within the counted grains, $N_{total\ pores}$ is the amount of the total pores within the counted grains (including occluded pores, pores at grain boundaries and pores at triple junctions). The results are presented in Table 4.

Table 4: The number density of occluded pores as a function of annealing time.

Sample	Annealing for 0 h (as sintered)	Annealing for 5 h
Mg-doped alumina	51%±12%	35%±16%
Co-doped alumina (Mg/Cr)	46%±6%	45%±8%

4.5 Grain Boundary Excess of Cr

Elemental analysis of the grain boundary region was conducted using STEM and EDS Figure 16-Figure 18. Al–Cr k-factor values were determined experimentally from the bulk of Cr- doped alumina according to equation (15). $k_{Cr,Al}$ was determined to be 0.93 considering our sample to be the standard in this case because we could determine the actual concentration of the elements by WDS.

EDS spectra of a line-scan perpendicular to the surface facet of pores is shown in Figure 18, clearly indicating the presence of Cr at the pores' surface. For quantitative analysis of the amount of Cr at the boundary and at the pore surface, EDS was acquired in STEM mode from a region rastered with the electron beam having dimensions of 85.65nm x 101.5nm.

To determine the excess of Cr at the grain boundary and the pore surface three EDS measurements were conducted while rastering the electron beam over a constant area of the sample; the first at the grain boundary/surface of the pore and two others from the adjacent bulk, as shown in Figure 17. After subtracting the Cr signal from the adjacent bulk, the excess of Cr at the grain boundary/surface of the pore was determined as shown in Table 5. The detection limit was determined using equation (14).

Table 5: The excess of Cr at grain boundary/ surface of the pore with the calculated detection limit of Cr.

Area	Detection limit [atom/nm^2]	Excess of Cr [atom/nm^2]
Grain boundary	3	37
Occluded pore	0.3	9
Pore at a triple junction	0.2	7
Pore at a grain boundary	0.1	21

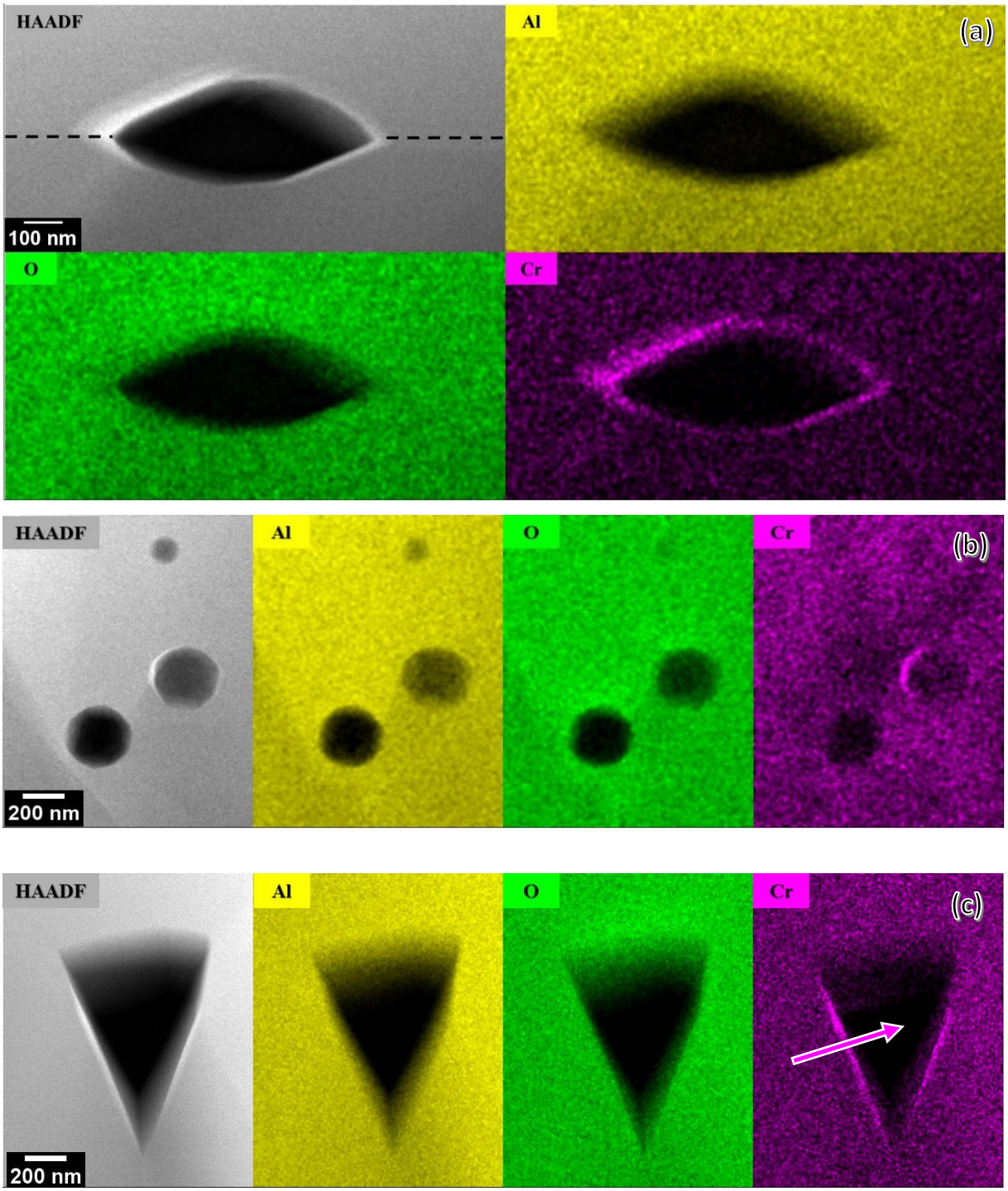

Figure 16: STEM micrographs of (a) a pore at a grain boundary, (b) occluded pores and (c) a pore at a triple junction.

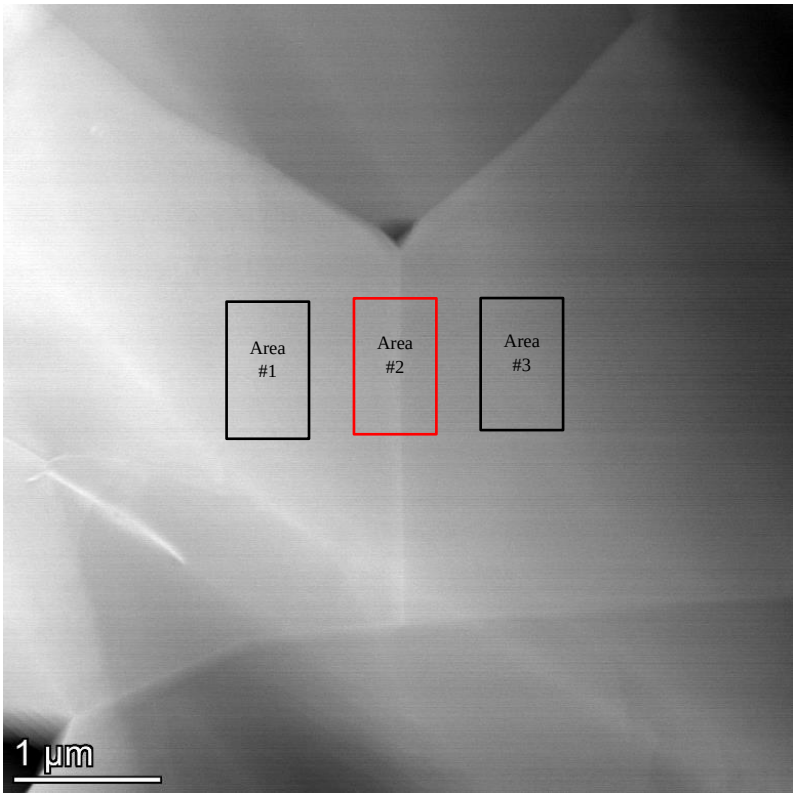

Figure 17: STEM micrograph of the grain boundary, showing regions for STEM-EDS analysis for the spatial difference method.

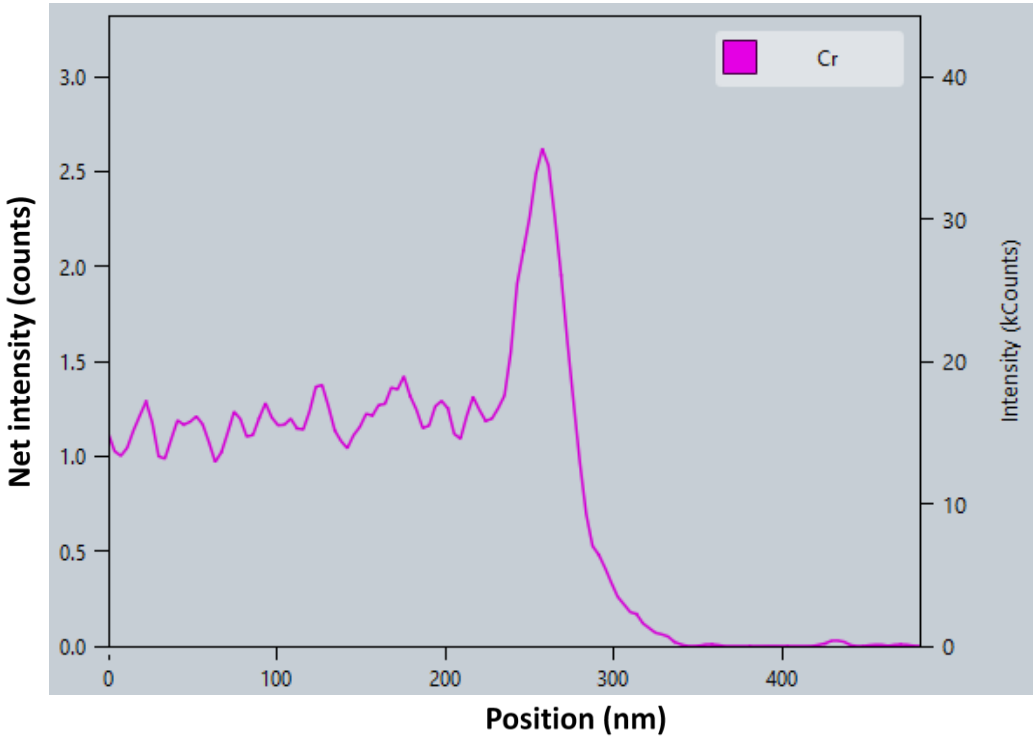

Figure 18: EDS line-scan across the pore surface indicated by the arrow in Figure 16(c).

5. Discussion

5.1 The Influence of Chromium on Densification of Alumina

It is important to be aware to the fact that during the sintering process, densification happens in parallel to grain growth and it is very hard to separate between the two phenomena. Therefore, obtaining dense material should be the first step to correctly analyze and understand the grain boundary mobility. The grain boundary mobility for all the samples were interpreted using raw data of samples which have relative density above 95% where at these levels of density, drag by residual pores has a negligible effect on the effective grain boundary mobility.

Densification during sintering is driven by the minimization of grain boundary energy relative to surface energy (replacement of free surfaces by grain boundaries). However, if the adsorption of an element results in a reduction of surface energy below that of the grain boundary energy, the driving force for sintering is nullified. Moreover, if the formation of an additional bulk phase beyond the solubility limit results in a film on the grain surface with a lower surface energy than the grain boundary energy, the driving force for sintering is similarly negated. These phenomena highlight the delicate interplay between surface and grain boundary energies and their influence on the densification process during sintering. As an example, alumina grain boundary energy ranges from 0.3-0.5 J/m^2 [51], while graphite surface energy is 0.064 J/ m^2 [52]. So having graphite film on the surface of an alumina grain would therefore hinder densification of alumina [53].

While the argument above is thermodynamic, clearly kinetic issues play a role during sintering. Bennison and Harmer suggested that Mg *increases* surface diffusion of alumina thus preventing pore detachment from a migrating grain boundary, and this will be beneficial to sintering [54].

In the current study it was noticed that Cr-doped alumina has more pores compared to undoped alumina. This finding match those mentioned in earlier studies [37, 38, 39, 40]. There are two main possible explanations for this result in the literature. The first is attributed to the weight loss of Cr_2O_3 in an oxidizing environment (PO_2=10^5 Pa to 10^2 Pa) above 1000°C due to evaporation of gaseous CrO_3 through a dissociation reaction [55,56]:

$$Cr_2O_{3\,(s)} + 1.5\ O_{2\,(g)} \rightarrow 2\ CrO_{3\,(g)} \qquad (19)$$

The second explanation, suggested by Nath et al., is attributed to the formation of a solid solution suggesting that it absorbs extra heat energy which results in less dense Al_2O_3–Cr_2O_3 compacts compared to undoped Al_2O_3 [39]. Although this argument has been proposed by some like Cui et al. and Yildiz et al., it lacks experimental justification [39, 40]. While this explanation may be thermodynamically viable, it does not offer a full explanation to explain pore detachment from grain boundaries and consequently the lower density seen in the literature regarding Cr doped alumina. Instead an alternative explanation based on the result from this study is provided in section (5.3).

A study conducted by Harabi and Davies and another conducted by Hirata suggest that the decrease in density can be attributed to the inhibition of alumina grain growth by Cr_2O_3 particles, which can hinder the rearrangement of alumina particles during sintering [38,42]. However, this explanation is incomplete because it doesn't take into consideration the fact that densification and grain growth are happening in parallel during sintering, primarily because it is difficult to determine how each mechanism influences the other during the sintering process.

In this work, we can attribute the reason for the decrease in density to the fact that there are many occluded pores in Cr-doped alumina compered to undoped alumina and the reason for the formation of so many occluded pores is apparently due to the effect of Cr on the surface diffusion where it decreases it, and this conclusion will be discussed later.

5.2 The Influence of Chromium on The Grain Boundary Mobility of Alumina

In this work it was found that chromium slows grain boundary mobility compared to undoped alumina and that the mobility decreases as the concentration of chromium increases. Given the Cr adsorption to grain boundaries (see Table 5), this is related to the solute drag effect [11] and is similar to the behavior of Mg in alumina [25].

The defect chemistry evaluated by Grimes, Atkinson et al., and Lagerlof et al. can be used to infer possible mechanisms for accelerated or decelerated grain-boundary mobility [57, 58, 59]. In the case of Mg, an interstitial mechanism (self-compensation) is energetically favorable as the solution mechanism. Given that Mg exists in alumina below its solubility limits, it can be inferred that doping alumina with MgO introduces interstitials not only within the bulk alumina

but also in the grain boundary region. It is postulated that the interstitials in the grain boundary region create a solute-drag force that reduces the mobility of the grain boundaries [25]. For Ca a vacancy formation mechanism is energetically favorable and required for charge compensation [60]. The increased mobility with Ca segregation is believed to be due to an increase in vacancy concentration in the vicinity of the grain boundaries, thus facilitating faster grain boundary motion [60].

However, there is a different trend when comparing Cr with these cations since Cr is iso-valent with Al. Thus, the only difference is cation size, and it is assumed that the larger size of the Cr cation at the grain boundary interferes with the mechanism of grain boundary motion (disconnection motion).

In reviewing the literature, no data was found on the influence of Cr on the grain boundary mobility of alumina while considering the separation between densification and grain growth during the sintering process. Manor reported that in the presence of Cr a distinct inhibition of grain growth occurs, however he didn't consider a dense sample [61]. The present study was done on fully dense samples, so the influence of Cr on grain growth kinetics in alumina can be separated from its influence on densification, and there will not be significant drag from pores. As Table 3 shows, there is a clear trend of reduction in the grain boundary mobility of alumina with increasing Cr concentration. The mechanism for grain boundary movement can be explained by disconnection motion. Disconnections are line defects at grain boundaries (or interfaces) and are defined by a dislocation and/or a step character [3, 59]. The presence of solute atoms at the grain boundary may influence the motion of disconnections.

Therefore, the observed decrease in the grain boundary mobility, apparently by solute drag [11], could be attributed to the influence of the adsorbing Cr cations on the types of active disconnections and/or on their mobility. It is not known if Cr increases the activation energy of disconnections formation, or if it slows the kinetics motion of the formed disconnections.

5.3 The Influence of Chromium on Pore Mobility

One of the most striking observations to emerge from the characterization of the samples in this work is the significant amount of occluded pores, in the Cr doped alumina and in the co-doped

alumina (Cr/Mg) compared to undoped alumina and Mg-doped alumina where the latter has the smallest amount of occluded pores which was also explained by Bennison and Harmer [54].

For a pore to move at the rate of a migrating grain boundary, surface diffusion of atoms in a direction opposite to motion of the grain boundary is required (and vacancy diffusion in the direction of grain boundary motion).While the strongest effect of MgO known to date is the retardation of grain boundary mobility, there is a secondary effect of MgO on pore mobility [24, 25]. Bennison et al. studied the role of the surface diffusivity because of Mg, and they showed that Mg adsorbed to free surfaces increases the surface diffusivity [54]. Considering the microstructure development map[1] (Figure 7), raising the surface diffusivity has an effect of shifting the pore-grain boundary separation region to larger grain size which is beneficial to sintering [13, 62].

Separation of pores from the boundary could either occur when the pore velocity (V_p) becomes less than the boundary velocity (V_b) or when the boundary velocity becomes higher than the pore velocity. The results, as shown in Table 3, indicate that Cr and Mg have the same effect on the grain boundary mobility, they impose a drag force on the boundary (solute drag). However, the results summarized in Table 4 suggest that for pore occlusion Cr does the opposite compared to Mg. The presence of Mg in alumina results in pores moving with the moving grain boundary, because the surface diffusion will dictate the pore mobility, which due to Mg is fast enough to move with the grain boundary. However, for Mg-Cr co-doped alumina, the influence of Mg on the occluded pores in the presence of Cr was found to be less pronounced, and more pores are occluded. These results provide wider support for the hypothesis that Cr apparently decreases surface diffusion in alumina.

Back to the microstructure development map, Figure 19 illustrates the effects of Mg and Cr on microstructure development in alumina according the findings of Bennison et al. and the current work [62]. The flattening of the grain size-density trajectory on doping with Mg or Cr is consistent with the experimental findings in which high densities are obtained with finer grain size. Also, the pore-grain boundary separation region is avoided in the case of doping with Mg while it become more critical when alumina is doped with Cr. Together these results provide crucial insights into the roles of Cr in alumina, one is the retardation of grain boundary mobility and second is decreasing surface diffusion.

[1] Such a map plots computed grain size-density trajectories for final-stage sintering where given transport mechanisms control sintering and defines the conditions under which pore-grain boundary separation occur.

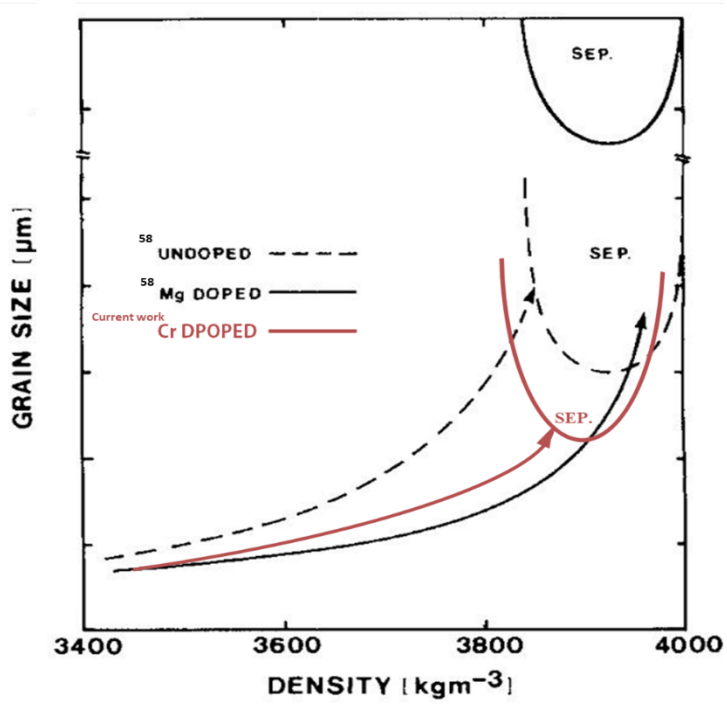

Figure 19: Microstructure development map for alumina illustrating the effect of raising the surface diffusivity and reducing the grain-boundary mobility. Redrawn based on [62] and the behavior of Cr doped alumina was added to this figure in red.

6. Summary and Conclusions

The aim of this research was to examine the impact of Cr on the effective mobility of grain boundaries in alumina. To achieve this goal, grain growth analysis was conducted on fully dense samples of undoped alumina and Cr/Mg doped alumina. The effective mobility of alumina grain boundaries was determined from samples that were doped with an increasing amount of Cr using parabolic growth behavior.

The results indicate that alumina doped with Cr exhibits reduced effective grain boundary mobility in comparison to undoped alumina, which is beneficial for grain growth during sintering. The mechanism by which Cr influences grain boundary mobility apparently by solute drag, similar to Mg.

Additionally, it was found that Cr-doped alumina contains considerably more occluded pores than either Mg-doped or undoped alumina. The excess of Cr found at pore surfaces in this study seems to reduce surface diffusion, resulting in an increased probability for grain boundary breakaway and pore occlusion. This is of course important in the densification process since annihilation of occluded pores will require bulk diffusion instead of relatively faster grain boundary diffusion for pores at grain boundaries.

To the best of our knowledge, this is the first time that the influence of Cr on the surface diffusion in alumina has been presented. In summary, the findings of this current research imply that Cr is beneficial only for grain growth, not for densification during sintering alumina.

7. Recommendations for Future Work

Grain growth is a basic phenomenon that takes place during the sintering process. However, the mechanism of grain growth is not yet comprehensively understood. Nonetheless, it's a significant aspect of microstructural development and it's crucial to regulate it. Therefore, it's essential to have a complete understanding of the mechanisms through which this process takes place.

While the defect chemistry evaluated by Grimes et al. [56] is used to explain possible mechanisms for accelerated or decelerated grain boundary mobility, with. Ca and Mg respectively, in the case of Cr this kind of charged defect does not exist. So while the motion of disconnections in the plane of grain boundaries could be hypothesized to be the mechanism of grain growth as it was shown previously by Sternlicht et al [5], the atomistic mechanism by which Cr influences the formation and/or motion of disconnections may be critical to fully understand the solute-drag phenomena.

Some of the grain boundaries and the free surfaces of the pores were more prone to Cr segregation than others (see Figure 16). Therefore, a correlation between planes/free surfaces and the segregating Cr is needed in order to understand the influence of Cr on the equilibrium crystal shape of alumina.

Finally, additional research is needed to establish the Cr evaporation rate during the sintering process.

8. References

1. P. W. Voorhees, 'The theory of Ostwald ripening, 'J. Stat. Phys., 38[1-2] 231-252 (1985).
2. Herbert Gleiter, "The mechanism of grain boundary migration." Acta Metallurgica 17(5), 565-573 (1969).
3. J. P. Hirth, and R. C. Pond, "Steps, dislocations and disconnections as interface defects relating to structure and phase transformations." Acta materialia, 44(12), 4749-4763(1996).
4 H. Sternlicht, W. Rheinheimer, M. J. Hoffmann, W. D. Kaplan, Journal of Materials Science, 51: 467-475 (2016).
5. J. Han, D. Srolovitz, M. Salvalaglio, "Disconnection-mediated migration of interfaces in microstructures: I. continuum model," Acta Materialia, 227, 117178 (2022).
6. J. Newman, P. S. Krishnaprasad, S. Ponczak, P. Brabant, "Modeling and Model Reduction for Control and Optimization of Epitaxial Growth in a Commercial Rapid Thermal Chemical Vapor Deposition Reactor," (1998).
7. M. N. Rahaman, "Sintering of Ceramics," CRC Press, pp. 580-582 (2008).
8. M. F. Yan, R. M. Cannon, H. K. Bowen, "Grain Boundary Migration in Ceramics," in Ceramic Microstructure '76, Fulrath RM, Pask JA, Boulder, editors CO: Westview Press, 1977, pp. 276-307.
9. K. Lücke, H. P. Stüwe, "On the Theory of Impurity Controlled Grain Boundary Motion," Acta Metallurgica, 19(10), 1087-1099 (1971).
10. M. Hillert, B. Sundman, "A Treatment of the Solute Drag on Moving Grain Boundaries and Phase Interfaces in Binary Alloys," Acta Metallurgica, 24(8), 731-743 (1976).
11. J. W. Cahn, "The impurity-drag effect in grain boundary motion," Acta Metallurgica, 10[9]: 789-798 (1962).
.12 J. D. Powers and A. M. Glaeser, "Grain Boundary Migration in Ceramics," Interface Science, 6[1-2]: 23-39 (1998).
.13 R. J. Brook, "Pore-grain boundary interactions and grain growth," Journal of the American Ceramic Society, 52: 56-57 (1969).
.14 J. Rödel and A. M. Glaeser, "Pore Drag and Pore-Boundary Separation in Alumina," Journal of the American Ceramic Society, 73[11]: 3302-3312 (1990).
15. I. Levin and D. Brandon, "Metastable Alumina Polymorphs: Crystal Structures and Transition Sequences," Journal of the American Ceramic Society, 81[8]: 1995-2012 (1998).
16. M. L. Kronberg, "Plastic deformation of single crystals of sapphire: basal slip and twinning," Acta Metallurgica, 5(9), 507-524 (1957).
17. D. Brandon, W. D. Kaplan, "Microstructural Characterization of Materials," John Wiley & Sons, Ltd (2008).
18. R.L. Coble. Transparent Alumina and Method of Preparation. US Patent Office US3026210A, (1962).
19. W.C Johnson, R.L Coble. "A Test of the Second-Phase and Impurity-Segregation Models for MgO Enhanced Densification of Sintered Alumina." Journal of the American Ceramic Society, 61[3-4]: 110–114, (1978).
.20 S.K. Roy, R.L. Coble, "Solubilities of Magnesia, Titania, and Magnesium Titanate in Aluminum Oxide", Journal of the American Ceramic Society. 51[1]: 1–6, (1968).
.21 J. Rödel, A.M. Glaeser, "Anisotropy of Grain Growth in Alumina". Journal of the American Ceramic Society, 73[11]: 3292-3301, (1990).
22. B. Hallstedt, "Thermodynamic Assessment of the System MgO–Al_2O_3", Journal of the American Ceramic Society, 75[6]: 1497–1507, (1992).
.23 L. Miller, A. Avishai, W.D. Kaplan, "Solubility Limit of MgO in Al_2O_3 at 1600°C", Journal of the American Ceramic Society. 89[1]: 350–353, (2006).

.24 S.J. Bennison, M.P. Harmer. “Effect of MgO solute on the kinetics of grain growth in Al_2O_3.” Journal of the American Ceramic Society, 66[5]: C-90, (1983).

.25 R. Akiva, A. Katsman, W.D. Kaplan, “Anisotropic Grain Boundary Mobility in Undoped and Doped Alumina”, Journal of the American Ceramic Society, 97[5]: 1610–1618, (2014).

26 C. A. Handwerker, P. A. Morris, R. L. Coble, “Effects of Chemical Inhomogeneities on Grain Growth and Microstructure in Al_2O_3”, Journal of the American Ceramic Society, 72[1]: 130-136, (1989).

27 K.A. McGowan. “Calcium aluminate clinker as a refractory aggregate with and without barium addition and use thereof”. US Patent Office 8123853 B2, (2012).

28 S.I. Bae, S. Baik, “Determination of Critical Concentrations of Silica and/or Calcia for Abnormal Grain Growth in Alumina”, Journal of the American Ceramic Society, 76[4]: 1065–1067, (1993).

29 Lee, C. H., KRÖGER, F. “Electrical Conductivity of Polycrystalline Al_2O_3 Doped with Silicon”. Journal of the American Ceramic Society, 68(2), 92-99(1985).

30. S.J. Dillon, M.P. Harmer, “Relating Grain Boundary Complexion to Grain Boundary Kinetics II: Silica-Doped Alumina”, Journal of the American Ceramic Society, 91[7]: 2314–2320, (2008).

31. R. Moshe, A. Berner, W.D. Kaplan, “The solubility limit of SiO_2 in α-alumina at 1600°C”, Scripta Materialia, [86]: 40–43, (2014).

32. C.A. Handwerker, P.A. Morris, R.L. Coble, “Effects of Chemical Inhomogeneities on Grain Growth and Microstructure in Al_2O_3”, Journal of the American Ceramic Society, 72[1]: 130–136, (1989).

33. R. Moshe and W.D. Kaplan, "The combined influence of Mg and Ca on microstructural evolution of alumina," Journal of the American Ceramic Society, 102: 4882-4887, (2019).

34. T.K. Parya, S. Banerjee, and M.B. Saha, "Densification of pure alpha alumina ceramics with chromia as dopant," Journal of the Indian Chemical Society, 89: 533-541, (2012).

35. R.D. Shannon, "Revised effective ionic radii and systematic studies of interatomic distances in halides and chalcogenides," Acta Cryst A, 32: 751-767, (1976).

36. A.F. Holleman and N. Wiberg, "Lehrbuch der anorganischen Chemie," 102. Aufl. Berlin: De Gruyter, (2007).

37. S-A. Cho, F.J. Arenas, and J. Ochoa, "Densification and hardness of Al_2O_3- Cr_2O_3 system with and without Ti addition," Ceramics International, 16: 301-309, (1990).

38 . T. Hirata, K. Akiyama, and H. Yamamoto, "Sintering behavior of Cr_2O_3- Al_2O_3 ceramics," Journal of the European Ceramic Society, 20: 195-199, (2000).

39. M. Nath, P. Kumar, A. V. Maldhure, S. Sinhamahapatra, K. Dana, A. Ghosh, et al., "Anomalous densification behavior of Al_2O_3- Cr_2O_3 system," Materials Characterization, 111: 8-13, (2016).

40. K. Cui, Y. Zhang, T. Fu, S. Hussain, T. Saad Algarni, J. Wang, et al., "Effects of Cr_2O_3 Content on Microstructure and Mechanical Properties of Al_2O_3 Matrix Composites," Coatings, 11: 234, (2021).

41. B. Kafkaslıoğlu Yıldız, H. Yılmaz, and Y. K. Tür, "Evaluation of mechanical properties of Al_2O_3- Cr_2O_3 ceramic system prepared in different Cr_2O_3 ratios for ceramic armor components," Ceramics International, 45: 20575-20582, (2019).

42. A. Harabi and T. J. Davies, "Densification and grain growth in sintered alumina-chromia powder mixtures," British Ceramic Transactions, 94: 97-102, (1995).

43. E. Manor, "Grain growth inhibition in nanocrystalline alumina doped with chromia," Nanostructured Materials, 8: 359-366, (1997).

44. J. J. Gulicovski, L. S. Čerović and S. K. Milonjić, "Point of Zero Charge and Isoelectric Point of Alumina," Materials and Manufacturing Processes, 23[6]: 615-619, (2008).

45. Lieberthal, M. and W.D. Kaplan, "Processing and Properties of Nanocomposites Reinforced with Sub-micron Ni and NiAl2O4," Materials Science and Engineering: A, 302[1]: 83-91, (2001).

46. A. Berner, F. Gimelfarb, and T. Ukhorskaya, "Metrological Aspects of Microprobe Analysis," Journal of Analytical Chemistry, 37[2]: 338-348, (1982).

47. J. Goldstein, D. E. Newbury, D. C. Joy, C. E. Lyman, P. Echlin, E. Lifshin, L. Sawyer, and J.R. Michael, "Scanning Electron Microscopy and X-ray Microanalysis," Plenum, NY, pp. 490-502, (1992).

48. V. J. Keast and D. B. Williams, "Quantification of Boundary Segregation in the Analytical Electron Microscope." J. Microsc., 199 [1] 45–55 (2000).

49. G. Cliff and G. W. Lorimer, "The quantitative analysis of thin specimens.", J Microsc., 103[2] 203-207 (1975).

50. M. I. Mendelson, "Average Grain Size in Polycrystalline Ceramics," Journal of the American Ceramic Society, 52[8]: 443-446, (1969).

51. J.D. Powers, A.M. Glaeser, "Grain Boundary Migration in Ceramics", Interface Science, 6: 23–39, (1998).

52. J. Lee, B. Lee, A simple method to determine the surface energy of graphite, Carbon letters, 21: 107–110, (2017).

53. L.Cohen, research thesis, " The High Temperature Solubility Limit of Carbon in Alumina", Technion, Haifa, Israel (2021)

54. S.J. Bennison and M.P. Harmer, "Effect of Magnesia Solute on Surface Diffusion in Sapphire and the Role-of Magnesia in the Sintering of Alumina" Journal of the American Ceramic Society, (1990).

55. P.D. Ownby and G.E. Jungquist, "Final sintering of Cr_2O_3", Journal of the American Ceramic Society, 55: 433-434, (1972).

56. H.C. Graham and H.H. Davis, "Oxidation/vaporization wettability of nickel, nickel-titanium alloys and nickel-kinetics of Cr_2O_3," Journal of the American Ceramic Society, 54: 89, (1971).

57. K. P. D. Lagerlöf and R. W. Grimes," The defect chemistry of sapphire (α-Al_2O_3)" Acta Mater, 46[16]: 5689-5700 (1998).

58. R. W. Grimes, "Solution of MgO, CaO, and TiO_2 in α-Al_2O_3" J. Am. Ceram. Soc., 77[2]: 378-384 (1994).

59. K. J. W. Atkinson, R. W. Grimes, M. R. Levy, Z. L. Coull and T. English," Accommodation of impurities in α-Al_2O_3, α-Cr_2O_3 and α-Fe_2O_3." J. Eur. Ceram. Soc., 23[16]: 3059-3070 (2003).

60. R. Moshe, W.D. Kaplan, The influence of CaO on alumina grain boundary mobility, Journal of the European Ceramic Society, **39**[4]:1324-1328, (2019).

61. E. Manor, Grain Growth Inhibition in Nanocrystalline Alumina Doped with Chromia, Nanostructured Materials 8, 359-366 (1997).

62. J. Bennison, "Effect of MgO on the Sintering of High Purity α- Al_2O_3"; Ph.D. Dissertation. Lehigh University, Bethlehem, PA, (1987).